Near-inertial wave dispersion by geostrophic flows

Jim Thomas[1,†]**, K. Shafer Smith**[1] **and Oliver Bühler**[1]

[1]Courant Institute of Mathematical Sciences, New York University, New York, NY 10012, USA

We investigate theoretically and numerically the modulation of near-inertial waves by a larger-amplitude geostrophically balanced mean flow. Because the excited wave is initially trapped in the mixed layer, it projects onto a broad spectrum of vertical modes, each mode n being characterized by a Burger number, Bu_n, proportional to the square of the vertical scale of the mode. Using numerical simulations of the hydrostatic Boussinesq equations linearized about a prescribed balanced background flow, we show that the evolution of the wave field depends strongly on the spectrum of Bu_n relative to the Rossby number of the balanced flow, ϵ, with smaller relative Bu_n leading to smaller horizontal scales in the wave field, faster accumulation of wave amplitude in anticyclones and faster propagation of wave energy into the deep ocean. This varied behaviour of the wave may be understood by considering the dynamics in each mode separately; projecting the linearized hydrostatic Boussinesq equations onto modes yields a set of linear shallow water equations, with Bu_n playing the role of the reduced gravity. The wave modes fall into two asymptotic regimes, defined by the scalings $Bu_n \sim O(1)$ for low modes and $Bu_n \sim O(\epsilon)$ for high modes. An amplitude equation derived for the former regime shows that vertical propagation is weak for low modes. The high-mode regime is the basis of the Young & Ben Jelloul (*J. Mar. Res.*, vol. 55, 1997, pp. 735–766) theory. This theory is here extended to $O(\epsilon^2)$, from which amplitude equations for the subregimes $Bu_n \sim O(\epsilon^{1/2})$ and $Bu_n \sim O(\epsilon^2)$ are derived. The accuracy of each approximation is demonstrated by comparing numerical solutions of the respective amplitude equation to simulations of the linearized shallow water equations in the same regime. We emphasize that since inertial wave energy and shear are distributed across vertical modes, their overall modulation is due to the collective behaviour of the wave field in each regime. A unified treatment of these regimes is a novel feature of this work.

Key words: quasi-geostrophic flows, rotating flows, waves in rotating fluids

1. Introduction

Internal gravity waves with frequencies close to the inertial frequency, termed 'near-inertial waves' (NIWs), dominate upper-ocean wave energy and shear (Garrett & Munk [1979]). They are preferentially excited by wind forcing and these fast

† Email address for correspondence: jthomas@cims.nyu.edu

motions are known to contain nearly half of the energy transferred to the ocean by atmospheric forcing (Pollard 1980). This energy may be exchanged with sufficiently strong geostrophic currents (Whitt & Thomas 2015), playing a role in the ocean's mesoscale energy balance. Moreover, downward propagation of NIW energy can lead to mixing via wave breaking in the thermocline (Alford *et al.* 2016), thus contributing to global-scale tracer distribution and transport.

Depending on the spatial variability of the wind stress and speed of propagation of storms over the upper ocean, the NIWs horizontal scales can vary between synoptic and mesoscales (Chelton *et al.* 2004, Silverthorne & Toole 2009). However, observations indicate that even in cases where synoptic-scale wind stress excites extremely large-scale NIWs, the wave field develops lateral spatial scales comparable to that of the pre-existing mesoscale eddy field as time progresses (Elipot, Lumpkin & Prieto 2010; Joyce *et al.* 2013). In such cases, it is typically assumed that the initial wave has the scale of the forcing, suggesting that the ocean eddy field modulates the wind-generated NIWs, imprinting the eddy horizontal scales on the wave field. Linear slab models of the type introduced by Pollard (1970) and Pollard & Millard (1970) can predict the observed rate of generation of upper-ocean near-inertial waves, but do not capture their spatial modulation. Moreover, the Pollard model predicts a vertical propagation rate far too small to account for the observed energy of near-inertial waves at depth.

The basic effect of the wave scale on its evolution can be understood by considering the standard dispersion relation and corresponding group velocity for hydrostatic inertia–gravity waves:

$$\omega^2 = f^2 \left(1 + Bu_{wave}\right), \quad Bu_{wave} = \frac{N^2 k_h^2}{f^2 k_z^2} \Rightarrow \frac{\partial \omega}{\partial k_z} = -\frac{N^2 k_h^2}{\omega k_z^3}, \quad (1.1a,b)$$

where the final expression above is the vertical group velocity, ω is the wave frequency, N is the buoyancy frequency, f is the Coriolis parameter and k_h and k_z are the horizontal and vertical wavenumbers. This highlights the importance of the waves' Burger number Bu_{wave}, which for the storm-generated NIWs is so small that all relevant frequencies are narrowly concentrated near the inertial frequency f. In addition, the waves' propagation into the deep ocean would be exceptionally slow, of the order of a few centimetres per day (Gill 1984). Observations in the Ocean Storms experiment, however, found that near-inertial waves excited by storms propagate into the deep ocean within days (D'Asaro *et al.* 1995), possibly consistent with a reduction in their horizontal scales by the eddy field, as in the observations mentioned above.

Assuming that the initial wave field is spatially homogeneous, i.e. infinite horizontal scale, we may consider a modified Burger number

$$Bu = \frac{N^2}{f^2 L^2 k_z^2}, \quad (1.2)$$

which naturally arises by non-dimensionalizing the governing equations using L as the horizontal scale, as is done in (1.6) below. In a landmark theoretical paper, Young & Ben Jelloul (1997, hereafter YBJ) used multi-time asymptotic analysis under the assumptions of $Bu \sim \epsilon$, where

$$\epsilon = \frac{V_g}{fL} \ll 1 \quad (1.3)$$

is the Rossby number based on the geostrophic velocity V_g, to derive an amplitude equation that describes the slow evolution of the wave field. The predicted wave propagation speed from the YBJ model is in accord with observations from the Ocean Storms experiment. By contrast, Klein & Treguier (1995), and later Danioux & Klein 2008, analysed a regime where $Bu \sim O(1)$, which keeps the (dispersive) pressure term at leading order. Is such a regime ever realized in the ocean? We will demonstrate that both scalings occur in the vertical spectrum of observed NIWs.

To clarify matters and make connection with the existing literature, we consider an idealized setting: an initial value problem consisting of a horizontally scale-free inertial oscillation superimposed on an eddy field that is assumed to be geostrophic, barotropic, steady and stronger than the wave field. The assumption of a barotropic eddy field is based on observations that indicate that NIWs have vertical scales that are of order the mixed layer depth (see, for example, Alford *et al.* 2016), small compared to the vertical scale of the eddy field, which is typically set by the pycnocline depth (Vallis 2006). Geostrophy is consistent with the small Rossby number that characterizes mid-latitude eddies, eddies that evolve on time scales of order weeks or longer. Finally, we assume that the eddy velocity amplitude is large compared to that of the waves, consistent with observed oceanic kinetic energy frequency spectra (see, e.g. Ferrari & Wunsch 2009). It should be noted, however, there are also indications that in some locations and times, the inertial field is stronger than the eddy field, which may lead to an energetic exchange between the eddy and wave fields (Xie & Vanneste 2015; Wagner & Young 2016).

With these assumptions, we consider the hydrostatic Boussinesq equations (hereafter referred to as simply Boussinesq equations)

$$\frac{\partial \boldsymbol{v}}{\partial t} + \hat{\boldsymbol{z}} \times \boldsymbol{v} + \left(\frac{N_0 H}{fL}\right)^2 \nabla p + \epsilon \left\{ \boldsymbol{V} \cdot \nabla \boldsymbol{v} + \boldsymbol{v} \cdot \nabla \boldsymbol{V} \right\} = 0, \tag{1.4a}$$

$$\frac{\partial b}{\partial t} + \tilde{N}^2(z)w + \epsilon \, \boldsymbol{V} \cdot \nabla b = 0, \tag{1.4b}$$

$$\frac{\partial p}{\partial z} = b, \tag{1.4c}$$

$$\nabla \cdot \boldsymbol{v} + \frac{\partial w}{\partial z} = 0, \tag{1.4d}$$

linearized with respect to a steady barotropic geostrophic eddy field,

$$\boldsymbol{V} = \hat{\boldsymbol{x}} U + \hat{\boldsymbol{y}} V = \hat{\boldsymbol{z}} \times \nabla \Psi, \tag{1.5}$$

where $\Psi = \Psi(x, y)$ is the geostrophic streamfunction. In (1.4), $\nabla = \hat{\boldsymbol{x}}\partial/\partial x + \hat{\boldsymbol{y}}\partial/\partial y$ is the horizontal gradient operator, $\boldsymbol{v} = \hat{\boldsymbol{x}} u + \hat{\boldsymbol{y}} v$ and w are the horizontal and vertical wave velocity components, p is the wave pressure, b the wave buoyancy, $\tilde{N}(z) = N(z)/N_0$ is the non-dimensional buoyancy frequency and f is the constant Coriolis frequency. (Although a variable Coriolis frequency is known to accelerate the vertical propagation of NIWs (Balmforth & Young 1999, Moehlis & Llewellyn Smith 2001), in the present work we shall focus attention on the modulation of waves due to a mean flow alone.) All variables are non-dimensionalized, with L the horizontal length scale of the geostrophic flow, H the depth of the fluid, V_g the geostrophic velocity scale and V_w the horizontal wave velocity scale. Perturbation vertical velocity is non-dimensionalized by $V_w H/L$, buoyancy by $N_0^2 V_w H/fL$ and

pressure follows from hydrostasy. Although we distinguish between wave (V_w) and eddy (V_g) velocity scales, for the linearized equations the magnitude of the wave velocity scale is arbitrary. The Rossby number, defined in (1.3), is the central small parameter.

Assuming rigid lid boundary conditions at the top and bottom of the domain, we project (1.4) onto baroclinic modes (see appendix A for details) to obtain a set of decoupled linear shallow water equations for each mode

$$\frac{\partial \boldsymbol{v}_n}{\partial t} + \hat{\boldsymbol{z}} \times \boldsymbol{v}_n + Bu_n \nabla p_n = -\epsilon \left\{ \boldsymbol{v}_n \cdot \nabla V + V \cdot \nabla \boldsymbol{v}_n \right\}, \tag{1.6a}$$

$$\frac{\partial p_n}{\partial t} - w_n = -\epsilon \ V \cdot \nabla p_n, \tag{1.6b}$$

$$\nabla \cdot \boldsymbol{v}_n + w_n = 0, \tag{1.6c}$$

where $Bu_n = (N_0 H/(\lambda_n f L))^2$ is the modified Burger number in (1.2) for the nth baroclinic mode and λ_n is the eigenvalue of the Sturm–Liouville equation involved in the projection (see (A 3a,b)). Recall that 'L' refers to the spatial scale of the background flow, which is the only horizontal length scale in the problem at $t = 0$. However, this does not necessarily mean that each vertical wave mode will acquire this length scale, but rather is expected to reach a scale based on the dynamical evolution of (1.6). Though not required for the analysis, for the sake of simplicity we take a constant buoyancy frequency, for which $\lambda_n = n\pi$ and therefore

$$Bu_n = \left(\frac{N_0 H}{n\pi f L} \right)^2. \tag{1.7}$$

Since the wave field corresponding to the barotropic mode ($n = 0$) remains as a trivial horizontally uniform inertial oscillation, we consider only the dynamics of baroclinic modes ($n \geqslant 1$) in this study. Note that in the absence of a background flow, the dispersion relation for the linear waves based on (1.6) is

$$\omega_n = \sqrt{1 + Bu_n |\boldsymbol{k}|^2}, \tag{1.8}$$

thus low-n modes, with $Bu_n \sim O(1)$, are more dispersive than higher modes, with $Bu_n \ll 1$ (this will motivate terminology introduced in the next section).

For a given Rossby number ϵ, the effect of the background flow on a particular mode is decided crucially by Bu_n. To understand this, first consider the case of higher baroclinic modes with $Bu_n \lesssim \epsilon$ (this is the limit considered by YBJ). For these modes, the $Bu_n \nabla p_n$ term in (1.6a) is asymptotically small so that it may be moved inside the curly braces on the right-hand side, which implies that wave dispersion arising due to the pressure gradient term is comparable to refraction and advection of the wave field by the mean flow. The left-hand side then contains an exact inertial wave operator of the form $(\partial/\partial t + \hat{\boldsymbol{z}} \times)$. The inertial wave field, excited by the initial data, interacts with the background flow via the terms on the right-hand side. Since the mean flow is steady, the right-hand side terms have frequency 1 (f in dimensional units), which can resonantly force the left-hand side, allowing for $O(1)$ modulations of the leading-order inertial wave field on time scales $t \gtrsim 1/\epsilon$. Looked at another way, modes with $Bu_n \lesssim \epsilon$ are excited by resonant wave–wave-geostrophic triads. It must however be noted that this form of resonant interaction is different from conventional resonant wave triads which satisfy resonance conditions between wavenumbers in addition to

frequencies (see for example Craik 1985). This is the origin of the YBJ amplitude equation, which will be derived for the shallow water system in §3. Related examples of similar dynamics can be found in, e.g. Falkovich (1992) and Falkovich, Kuznetsov & Medvedev (1994).

Now consider the case of lower baroclinic modes, that satisfy $Bu_n \sim 1$. For these modes, the pressure gradient term in (1.6a) remains in the leading-order equation. The left-hand side of (1.6a) is not an exact inertial wave operator in this case, and therefore even though homogeneous initial data excite inertial waves at leading order, and inertial wave-mean flow terms of frequency 1 arise on the right-hand side, these do not resonantly force the leading-order inertial wave field by the mechanism described above. Therefore, the leading inertial wave fields of these modes are not modulated by the eddies for time scales $1/\epsilon$ (although they are for times $\sim 1/\epsilon^2$, as we shall demonstrate). This was pointed out by Klein & Treguier (1995) using the linearized equations in a study of the interaction of a one-dimensional barotropic front with NIWs. In a similar setting, but for a different problem – namely the emergence of oscillations at $2f$ frequency in an initial value problem for a homogeneous wave field in the presence of a front – Danioux & Klein (2008) also observed the lack of NIW modulation by the eddy field in this regime.

We therefore expect the nature of the interaction to vary depending on the relationship between the modal Burger number and Rossby number: modes with $Bu_n \sim O(1)$ are expected to behave very differently from modes that satisfy $Bu_n \ll 1$. Because an inertial oscillation excited by winds will project onto a wide spectrum of vertical modes, each with different modal Burger number, we expect both limits to be relevant to the evolution of the wave field. We demonstrate this in §2, first showing the distribution of Bu_n expected for a typical surface-trapped wave field, then analysing numerical solutions of the linear Bousinnesq equations, (1.4), for an idealized background eddy field. To quantify the interactions, in §3 we use multiscale asymptotics to investigate a range of Burger–Rossby number scalings, deriving distinct amplitude equations for each; these are tested against numerical integrations of the shallow water equations for the particular mode under consideration. We also show that all the regimes with $Bu_n \ll 1$ can be obtained by a next-order expansion of the original YBJ amplitude equation, and this results in a set of 'improved' equations for the weak dispersion regimes. In §4 we use conservation laws for each asymptotic regime to explain the tendency toward increased concentration of NIWs in anticyclones, and the production of increasingly small scales in the wave field as the Burger number decreases. Finally, §5 summarizes our findings and concludes the present study.

2. The asymptotic regimes of NIW modulation

Our goal in this section is to motivate the existence of different asymptotic regimes in which the modulation of the wave field by the mean flow can vary significantly. As mentioned, Bu_n decreases from $O(1)$ for low modes to asymptotically small values for high modes, which means that wave energy and shear in real flows, which project onto a broad spectrum of modes, are distributed across interaction regimes ranging in dispersive strength. The cumulative effects of the background flow on NIWs depends on the distribution of Bu_n with respect to the Rossby number.

Consider a hypothetical storm-generated inertial wave horizontal velocity field, in complex form,

$$\mathscr{U} = u + \mathrm{i}v = A(z)\mathrm{e}^{-\mathrm{i}t}, \quad \text{with } A(z) = \exp\left(\frac{-z^2}{2h^2}\right), \tag{2.1}$$
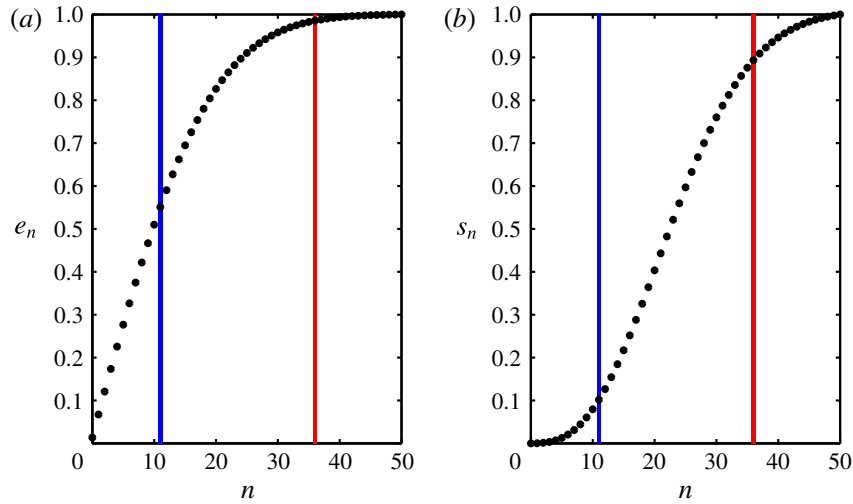
FIGURE 1. (Colour online) Fractional energy e_n and fractional shear s_n contained in the first 50 baroclinic modes. The blue and red curves correspond to $n_{0.125} \approx 11$ and $n_{0.0125} \approx 36$, respectively, calculated based on (2.5). These curves demarcate between modes with stronger dispersion $Bu_n \gg \epsilon$ in (a) and weak dispersion modes with $Bu_n \leqslant \epsilon$ in (b). For example, if $\epsilon = 0.0125$ (red line) then most of the wave energy and almost all of the wave shear is associated with strongly dispersive modes. Conversely, if $\epsilon = 0.125$ (blue line) only about half of the energy and less than 10 % of the shear are associated with strongly dispersive modes. This illustrates the sensitivity of the relevant modal regimes to the Rossby number ϵ.

where $z = -h$ is the depth at which the inertial shear, $A'(z)$, is maximal and where $z = 0$ is the surface. This is an exact solution to the linear equations without a balanced flow. Projecting (2.1) onto baroclinic modes one obtains (see appendix A for details)

$$A(z) = \frac{A_0}{2} + \sum_{n=1}^{\infty} A_n \cos\left(\frac{n\pi z}{H}\right), \quad A_n = \frac{2}{H} \exp\left(-\frac{\pi^2 n^2 h^2}{2H^2}\right) \int_{-H}^{0} \exp\left(-\frac{z^2}{2h^2}\right) \, \mathrm{d}z,$$

(2.2a,b)

and in the limit $h \ll H$, the coefficients are approximately

$$A_n \approx \frac{\sqrt{2\pi}h}{H} \exp\left(-\frac{\pi^2 n^2 h^2}{2H^2}\right).$$

(2.3)

The fractions of total energy and total shear contained in the first n baroclinic modes are

$$e_n = \frac{\displaystyle\sum_{j=1}^{n} A_j^2}{\displaystyle\sum_{j=1}^{\infty} A_j^2} \quad \text{and} \quad s_n = \frac{\displaystyle\sum_{j=1}^{n} B_j^2}{\displaystyle\sum_{j=1}^{\infty} B_j^2},$$

(2.4a,b)

where $B_j = (j\pi/H)A_j$ corresponds to the Fourier coefficients of $A'(z)$. Figure 1 shows e_n and s_n, assuming an eddy length scale $L = 40$ km, ocean depth $H = 5$ km, buoyancy frequency $N = 100f = 10^{-2}$ s^{-1} and shear depth $h = -75$ m. Motivated by

the observations of wind-excited NIWs discussed in D'Asaro *et al.* (1995), we also chose the balanced flow velocity $V_g = 0.05$ m s^{-1} which gives $\epsilon = 0.0125$. For the numerical experiments that follow, we choose a second Rossby number, $\epsilon = 0.125$, an order of magnitude larger than the previous one. As mentioned before, the strength of modulation of the wave field by the mean flow is expected to depend on the fraction of modes with $Bu_n \sim \epsilon$, where advection–refraction and dispersion coincide in strength. We construct a critical mode number for a given Rossby number as

$$n_\epsilon = \frac{N_0 H}{\pi f L \sqrt{\epsilon}} \tag{2.5}$$

by equating modal Burger number (1.7) and Rossby number. The coloured vertical lines in figure 1 indicate $n_{0.125}$ and $n_{0.0125}$. Notice that for the lower Rossby number case, fewer modes satisfy $Bu_n \lesssim \epsilon$ and therefore less energy is associated with the regime $Bu \sim \epsilon$, as discussed before.

We now turn to some idealized simulations to validate our qualitative predictions. To illustrate that the modulation of the wave field depends strongly on the fraction of modes that satisfy $Bu_n \sim \epsilon$ versus those that satisfy $Bu_n \sim O(1)$, we numerically integrate the linear Boussinesq equations (1.4) by projecting onto the first 150 baroclinic modes and using the initial data

$$u = \exp\left(\frac{-z^2}{2h^2}\right), \quad v = p = b = 0 \quad \text{at } t = 0, \tag{2.6a,b}$$

with $h = -75$ m. This initial condition in the absence of a mean flow will excite an inertial wave field of the form (2.1). In order to make explicit the dependence on Rossby number, we consider two experiments, with Rossby numbers $\epsilon = 0.0125$ and 0.125. The background eddy flow streamfunction is

$$\Psi = \sin x \sin y. \tag{2.7}$$

We note that our experimental set-up is extremely idealized, imposing a constant value for N and a surface intensified inertial wave of the form (2.1), which is supposed to mimic an inertial wave field trapped in the mixed layer of the upper ocean. Nevertheless, since our goal is to give a simple illustration of the dependence of the resonant modulation of NIWs on the parameter regime, we persist with this simple set-up. The simulation was performed with a pseudospectral code, using fourth-order Runge–Kutta time stepping and 128^2 Fourier modes. A hyperdiffusion operator of the form $-\nu \Delta^4 v_n$ with $\nu = 10^{-12}$ was added to the right-hand side of the momentum equation for numerical stability.

Figure 2(*a–f*) shows the horizontal distribution of wave kinetic energy, integrated vertically over the top 100 m for each of the two simulations, at times $2.5/\epsilon$, $5/\epsilon$ and $7.5/\epsilon$ (normalized by their respective Rossby numbers). One can immediately see, especially in the larger Rossby number case (*d–f*), an expulsion of wave energy from cyclonic vorticity regions of the background flow and trapping of waves in anticyclonic vorticity regions. The wave energy is redistributed both horizontally into anticyclonic regions, and downward, as can be seen in panels (*g,h*), which show time series of the horizontally averaged and vertically integrated kinetic energy in the upper 100 m for each simulation. In the larger Rossby number case, after 80 days almost 93 % of the initial energy has left the top 100 m, whereas after an order of magnitude longer time (800 days), only 29 % of the initial energy leaves
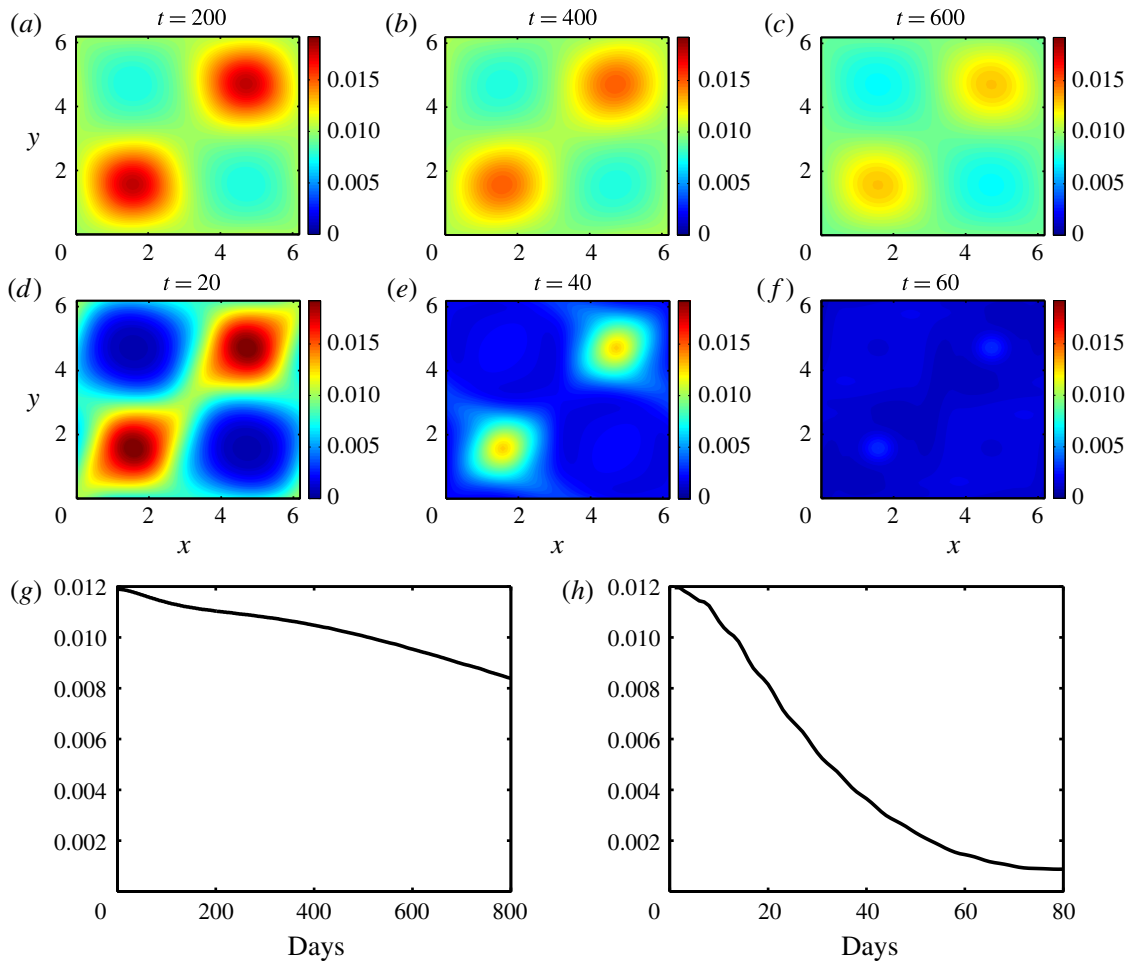
FIGURE 2. (Colour online) (*a–c*) Kinetic energy of the first 150 baroclinic modes integrated over the top 100 m of the model domain for the simulation with $\epsilon = 0.0125$ at times $2.5/\epsilon$, $5/\epsilon$ and $7.5/\epsilon$. (*d–f*) Same for simulation with $\epsilon = 0.125$. Both cases show an accumulation of wave energy in anticyclonic regions ([0, π] × [0, π] and [π, 2π] × [π, 2π] for the streamfunction (2.7)), with stronger accumulation in the case of larger ϵ. (*g,h*) Horizontally averaged and vertically integrated kinetic energy in the top 100 m of the model domain for simulations with $\epsilon = 0.0125$ (*g*) and $\epsilon = 0.125$ (*h*).

the upper ocean for the case $\epsilon = 0.0125$. This is the 'inertial chimney effect' (Lee & Niiler 1998), the mechanism by which anticyclonic vorticity regions act as conduits for inertial energy to reach the thermocline. We note that we were able to obtain this phenomenon, consistently observed in numerical simulations using more complex models (Zhai, Greatbatch & Zhao 2005; Zhai, Greatbatch & Eden 2007), in the most basic set-up – using linearized interaction equations.

The stronger tendency for anticyclonic accumulation and downward wave energy propagation for the case with $\epsilon = 0.125$ is consistent with the inference from figure 1 that with larger Rossby number, more modes satisfy $Bu_n \ll 1$, which suppresses the dispersive pressure term in the leading-order dynamics, resulting in strong modulation of NIWs by the background flow and rapid vertical propagation. For smaller Rossby numbers, most of the wave energy is in modes that satisfy $Bu_n \sim O(1)$ leading to less modulation and thus weaker vertical propagation of NIWs.
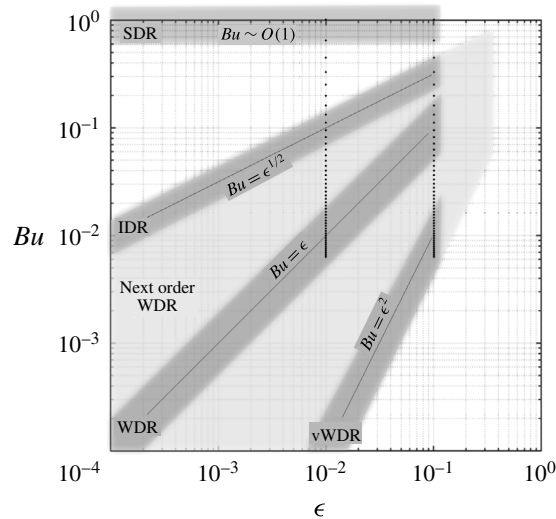
FIGURE 3. Dispersion regimes for rotating shallow water. The dark grey regions denote the four subregimes developed in § 3; boundaries of each region are fuzzy, to emphasize that the regions are not precisely defined. The region at the top is SDR, with $Bu \sim O(1)$, and the region along the diagonal is WDR: the YBJ regime, with $Bu \sim \epsilon$. The subregimes IDR ($Bu \sim \epsilon^{1/2}$) and vWDR ($Bu \sim \epsilon^2$) are also shown. The WDR region is bound on the right by $\epsilon \approx 10^{-1}$, as a canonical small value. The light grey region denotes the next-order WDR equation (3.17), bounded by $Bu \sim \epsilon^2$ and $Bu \sim \epsilon^{1/2}$, capturing all possible balances of terms in the equation. The right side boundary is $\epsilon \approx 10^{-1/2}$, so that the smallest terms, which scale like $\epsilon^2 \approx 10^{-1}$, are still 'small'. The vertical dotted lines represent values of Bu_n for $n = 1, \ldots, 50$, $L = 40$ km, $f = 10^{-4}$ s^{-1}, $N = 100f$ and $H = 5$ km, at two different values of ϵ. The point is to show the range of regimes necessary to describe how the problem changes with Rossby number.

To capture these dynamics, we consider two broad scalings: (i) the 'strong dispersion regime' (SDR) with $Bu_n \sim O(1)$ and (ii) the 'weak dispersion regime' (WDR) with $Bu_n \ll 1$, with names motivated by terminology introduced in Danioux & Klein (2008) and discussed below (1.8). The latter regime, which Klein & Llewellyn Smith (2001) also identify as the 'trapping regime', was investigated in detail by YBJ.

Notice that for very small Rossby numbers, there may also be modes with Bu_n that are asymptotically small but still large compared to ϵ. Moreover, for larger Rossby numbers, there may be modes with $Bu_n \sim O(\epsilon^2)$. This can be seen in figure 3, which attempts to delineate the asymptotic regimes discussed above, as well as some new subregimes. The vertical dotted lines represent Bu_n for $n = 1$–50, with the same parameters used in the analysis above, for two different values of ϵ. One can see that in both cases, there are many modes that do not lie within the formal ranges of validity of the SDR or WDR. However, we will show in the next section that a next-order expansion about the distinguished limit $Bu_n \sim \epsilon$ provides correction terms for the cases where Bu_n, while still small, is asymptotically large or small compared to ϵ, as denoted by the lighter grey region called 'next order WDR'. At the edges of this regime are subregimes defined by $Bu_n \sim \epsilon^{1/2}$ and $Bu_n \sim \epsilon^2$, which we refer to, respectively, as the 'intermediate dispersion regime' (IDR) and 'very weak dispersion regime' (vWDR). For larger ϵ, most modes lie deep in the WDR, and span both its subregimes, IDR and vWDR. For smaller ϵ, more modes lie in the IDR. Details of these limiting cases will be discussed in § 3.

3. Amplitude equations for strong and weak dispersion regimes

Here we consider asymptotic approaches to understanding the range of behaviours for different vertical modes seen in the last section. Keeping in mind that the following analysis holds for specific baroclinic modes, we suppress the subscript n; for instance we represent modal Burger number as Bu instead of Bu_n, wave amplitude as A instead of A_n and so on. We rewrite (1.6) as

$$\frac{\partial \boldsymbol{v}}{\partial t} + \hat{\boldsymbol{z}} \times \boldsymbol{v} + Bu\nabla p + \epsilon \left\{ \boldsymbol{v} \cdot \nabla V + V \cdot \nabla \boldsymbol{v} \right\} = 0, \tag{3.1a}$$

$$\frac{\partial p}{\partial t} + \nabla \cdot \boldsymbol{v} + \epsilon \, V \cdot \nabla p = 0. \tag{3.1b}$$

We impose periodic boundary conditions in the horizontal and set the initial conditions to

$$u = \text{constant}, \quad v = p = 0 \quad \text{at} \quad t = 0 \tag{3.2a,b}$$

so that spatially homogeneous inertial oscillations are excited. Because the analysis that follows assumes a single length scale for the background flow, we use the idealized streamfunction (2.7), representing a single dominant mode of the background flow.

Using the method of multiple time scales, in the coming subsections we derive amplitude equations for NIW modes with different Bu–ϵ scalings. We note that although we assume a steady mean flow throughout, the derivation of the amplitude equations requires only a time scale separation between the mean flow and NIWs and therefore the derivations retain their validity if the mean flow is slowly evolving rather than steady. These amplitude equations will be compared with numerical solutions to the linear rotating shallow water equations, (3.1) (hereafter RSW). As with the linear Boussinesq simulation discussed in § 2, the codes used to solve the linear shallow water equations were pseudospectral with fourth-order Runge–Kutta time stepping. A hyperdiffusion operator of the form $-\nu\Delta^4 \boldsymbol{v}$ was added to the momentum equations in the shallow water equations, and to the amplitude equations in various regimes for numerical stability. The resolution necessary for convergence of the numerical solutions varied based on the asymptotic regime considered. For example 256^2 or 512^2 Fourier modes were necessary in order to capture the formation of small-scale features in vWDR whereas 128^2 Fourier modes were sufficient in other regimes. Hyperviscosity was varied according to the resolution so as to obtain $O(1)$ Reynolds number at the grid scale, with $\nu = 10^{-12}$ at lowest resolution. Convergence was checked by doubling the resolution and decreasing the time steps.

3.1. *The weak dispersion regime*

'Weak dispersion' refers to the suppression of the pressure term (which leads to wave dispersion) at leading order in (3.1a) when $Bu \ll 1$. This defines the broad set of dynamics that, as argued above, characterizes higher baroclinic modes. For expository reasons, we discuss this regime first, and the low-mode case of $Bu \sim O(1)$ later. To proceed asymptotically in the weak dispersion regime, one needs to assume a particular scaling between Bu and the defining small parameter, ϵ. YBJ exploited the distinguished limit $Bu \sim O(\epsilon)$ to derive an amplitude equation for the evolution of NIWs. We consider the same scaling to derive an improved equation for the weak dispersion regime, noting that this distinguished scaling retains the largest number of terms entering at asymptotically higher orders.

Following YBJ, it is convenient to switch to complex coordinates

$$\mathscr{U} = u + \mathrm{i}v \quad \text{and} \quad \xi = x + \mathrm{i}y \tag{3.3a,b}$$

from which it follows that $\partial/\partial x + i\partial/\partial y = 2\partial/\partial\xi^*$, $U + iV = 2i\,\partial\Psi/\partial\xi^*$, $\nabla \cdot \boldsymbol{v} = \partial\mathscr{U}/\partial\xi + \text{c.c.}$ and $\boldsymbol{v} \cdot \nabla = \mathscr{U}\partial/\partial\xi + \text{c.c.}$ For convenience later, we also define the operators

$$\Delta \equiv \frac{\partial^2}{\partial x^2} + \frac{\partial^2}{\partial y^2} = 4\frac{\partial^2}{\partial\xi\partial\xi^*} \quad \text{and} \quad \Delta^\perp \equiv \frac{\partial^2}{\partial x^2} - \frac{\partial^2}{\partial y^2} + 2i\frac{\partial^2}{\partial x\partial y} = 4\frac{\partial^2}{\partial\xi^{*2}}, \quad (3.4a,b)$$

the first of which is just the horizontal Laplacian. For the second operator we note a physical interpretation by observing that

$$|\Delta^\perp\Psi|^2 = \left(\frac{\partial^2\Psi}{\partial x^2} - \frac{\partial^2\Psi}{\partial y^2}\right)^2 + 4\left(\frac{\partial^2\Psi}{\partial x\partial y}\right)^2 = \left(\frac{\partial V}{\partial x} + \frac{\partial U}{\partial y}\right)^2 + \left(\frac{\partial U}{\partial x} - \frac{\partial V}{\partial y}\right)^2 = \sigma^2, \tag{3.5}$$

where σ is the total mean horizontal shear (containing normal and tangential components). We also define the slow advection operator

$$\frac{\mathrm{D}}{\mathrm{D}T} = \frac{\partial}{\partial T} + \boldsymbol{V} \cdot \nabla = \frac{\partial}{\partial T} + J(\Psi, \ ). \tag{3.6}$$

Letting $T = \epsilon t$ be the slow time so that time derivatives become $\partial/\partial t \to \partial/\partial t + \epsilon\partial/\partial T$, we add the u equation to i times the v equation in (3.1a) to obtain

$$\frac{\partial\mathscr{U}}{\partial t} + i\mathscr{U} + \epsilon\left[\frac{\mathrm{D}\mathscr{U}}{\mathrm{D}T} + \frac{i}{2}\left(\Delta\Psi\ \mathscr{U} + \Delta^\perp\Psi\ \mathscr{U}^*\right) + 2\frac{Bu}{\epsilon}\frac{\partial p}{\partial\xi^*}\right] = 0, \tag{3.7a}$$

$$\frac{\partial p}{\partial t} + \frac{\partial\mathscr{U}}{\partial\xi} + \frac{\partial\mathscr{U}^*}{\partial\xi^*} + \epsilon\frac{\mathrm{D}p}{\mathrm{D}T} = 0. \tag{3.7b}$$

Expanding variables as

$$(\mathscr{U}, p) = (\mathscr{U}_0, p_0) + \epsilon(\mathscr{U}_1, p_1) + \epsilon^2(\mathscr{U}_2, p_2) + \cdots \tag{3.8}$$

the leading-order equations are

$$\frac{\partial\mathscr{U}_0}{\partial t} + i\mathscr{U}_0 = 0, \tag{3.9a}$$

$$\frac{\partial p_0}{\partial t} + \frac{\partial\mathscr{U}_0}{\partial\xi} + \frac{\partial\mathscr{U}_0^*}{\partial\xi^*} = 0, \tag{3.9b}$$

which have solutions

$$\mathscr{U}_0 = A_0\mathrm{e}^{-it}, \quad p_0 = -i\frac{\partial A_0}{\partial\xi}\mathrm{e}^{-it} + \text{c.c.} \tag{3.10a,b}$$

where $A_0 = A_0(\xi, \xi^*, T)$. Using the leading-order solutions (3.10a,b), the equations at $O(\epsilon)$ are

$$\frac{\partial\mathscr{U}_1}{\partial t} + i\mathscr{U}_1 + \left[\frac{\mathrm{D}A_0}{\mathrm{D}T} + \frac{i}{2}\left(\Delta\Psi\ A_0 - \frac{Bu}{\epsilon}\Delta A_0\right)\right]\mathrm{e}^{-it}$$

$$+ \frac{i}{2}\left[\Delta^\perp\Psi\ A_0^* + \frac{Bu}{\epsilon}\ \Delta^\perp A_0^*\right]\mathrm{e}^{it} = 0, \tag{3.11a}$$

$$\frac{\partial p_1}{\partial t} + \frac{\partial\mathscr{U}_1}{\partial\xi} + \frac{\partial\mathscr{U}_1^*}{\partial\xi^*} + \frac{\mathrm{D}}{\mathrm{D}T}\left(-i\frac{\partial A_0}{\partial\xi}\mathrm{e}^{-it} + \text{c.c.}\right) = 0. \tag{3.11b}$$
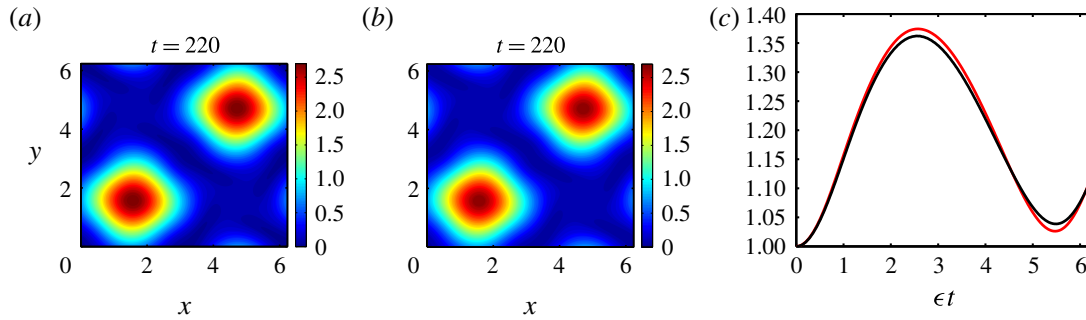
FIGURE 4. (Colour online) (a,b) $|A| = \sqrt{u^2 + v^2}$ obtained from the YBJ equation (3.12) and from RSW (3.1). (c) $\sqrt{\langle |A|^2 \rangle^{part}}$ versus slow time, ϵt, for the YBJ amplitude equation (red curve) and for RSW (black curve) where $\langle \phi \rangle^{part}$ refers to spatial average calculated over the top right quarter of the domain. The simulations used the parameters $\epsilon = Bu = 0.0125$.

Eliminating secular growth in (3.11a) by setting to zero the terms multiplied by e^{-it}, we obtain the shallow water version of the YBJ amplitude equation

$$\frac{\partial A_0}{\partial T} + J(\Psi, A_0) + \frac{i}{2}\left((\Delta \Psi)A_0 - \frac{Bu}{\epsilon}\Delta A_0 \right) = 0. \tag{3.12}$$

Note that in the slow time T, all terms in this expression are of the same asymptotic order; when $T = \epsilon t$ is used, all terms except the time derivative are of $O(\epsilon)$. Figure 4 compares the numerical solution of (3.12) with that of RSW for $Bu = \epsilon = 0.0125$. The amplitude equation agrees quite well with the parent model in detail. Note also the expected accumulation of wave activity in regions of anticyclonic vorticity.

3.2. *Next-order weak dispersion regimes*

Here we continue to the next order in ϵ to provide an amplitude equation that allows for a wider range of scalings between the Burger and Rossby numbers, consistent with the results in § 2. The usefulness of this exercise will be demonstrated after the derivation.

We will first need the solution to (3.11), given A_0 from (3.12). The result is

$$\mathcal{U}_1 = A_1 e^{-it} + B_1 e^{it}, \quad p_1 = -\left[i\left(\frac{\partial A_1}{\partial \xi} + \frac{\partial B_1^*}{\partial \xi^*} \right) + \frac{D}{DT}\frac{\partial A_0}{\partial \xi} \right] e^{-it} + \text{c.c.} \tag{3.12a,b}$$

where

$$B_1 = -\frac{1}{4}\left(\Delta^{\perp}\Psi \ A_0^* + \frac{Bu}{\epsilon}\Delta^{\perp}A_0^* \right). \tag{3.13}$$

To obtain a higher-order amplitude equation, we employ a 'composite' technique that proceeds as follows. The solvability condition (3.12) is modified as

$$\frac{DA_0}{DT} + \frac{i}{2}\left((\Delta \Psi)A_0 - \frac{Bu}{\epsilon}\Delta A_0 \right) = \epsilon \Phi, \tag{3.14}$$

where $\Phi = \Phi(x, T)$ (or $\Phi(\xi, \xi^*, T)$ in terms of complex coordinates) is a higher-order correction term. This is analogous to the derivation of higher-order correction terms for the nonlinear Schrödinger equation, which is the lower-order equation, to capture the evolution of deep water waves to a higher level of accuracy (see Dysthe 1979; Trulsen & Dysthe 1996). The reader may refer to Ablowitz (2011) for similar problems that take advantage of this composite method. An alternative approach is to define a second slow time, $\tau = \epsilon^2 t$ and derive an amplitude equation on time scales $\tau \sim O(1)$. Such a strategy, it can be shown, is equivalent to the above method and would result in the same slow amplitude equation on $1/\epsilon^2$ time scales (see, for example, appendix A of Thomas (2016) for a comparison of these two alternative methods). To obtain Φ, we need to prevent secular growth at the next order. At $O(\epsilon^2)$, (3.7a) gives

$$\frac{\partial \mathscr{U}_2}{\partial t} + i\mathscr{U}_2 + \Phi e^{-it} + \frac{D\mathscr{U}_1}{DT} + \frac{i}{2}\left(\Delta\Psi\mathscr{U}_1 + \Delta^\perp\Psi\mathscr{U}_1^*\right) + 2\frac{Bu}{\epsilon}\frac{\partial p_1}{\partial \xi^*} = 0. \quad (3.15)$$

Substituting the first-order solutions (3.12a,b) into the above and setting terms proportional to e^{-it} to zero, we obtain the solvability condition

$$\Phi + \frac{DA_1}{DT} + \frac{i}{2}\left(\Delta\Psi A_1 + B_1^*\Delta^\perp\Psi\right) - \frac{Bu}{2\epsilon}\left[i\Delta A_1 + i\Delta^\perp B_1^* + 4\frac{\partial}{\partial\xi^*}\left(\frac{D}{DT}\frac{\partial A_0}{\partial\xi}\right)\right] = 0. \quad (3.16)$$

We then eliminate Φ by combining the two equations as (3.14) + ϵ (3.16), use (3.13) to eliminate B_1, (3.12) to eliminate the $\partial^2 A_0/\partial T\partial\xi$ term and define a combined amplitude as $A = A_0 + \epsilon A_1$ to obtain the composite amplitude equation

$$\frac{\partial A}{\partial T} + J(\Psi, A) + \frac{i}{2}\Delta\Psi A - \frac{Bu}{\epsilon}\frac{i}{2}\Delta A - \frac{i}{8}\frac{Bu^2}{\epsilon}\Delta^2 A - \frac{i}{8}\epsilon|\Delta^\perp\Psi|^2 A + 2BuG = 0, \quad (3.17)$$

where

$$G = \frac{\partial}{\partial\xi^*}J\left(\frac{\partial\Psi}{\partial\xi}, A\right) + i\frac{\partial^2}{\partial\xi^{*2}}\left(\frac{\partial^2\Psi}{\partial\xi^2}A\right) - i\left(\frac{\partial^2\Psi}{\partial\xi^{*2}}\right)\frac{\partial^2 A}{\partial\xi^2} + \frac{i}{8}\Delta\left(\Delta\Psi A\right). \quad (3.18)$$

We may further set $T = \epsilon t$ in (3.17) resulting in a multiplication of every term besides the time derivative by ϵ (likewise for (3.12)).

Notice that (3.17) contains all the terms from (3.12), in addition to new correction terms of orders Bu^2/ϵ, ϵ and Bu. While typically one would seek a higher-order equation in order to extend the temporal range of validity of the model, or to improve accuracy at large values of the small parameter, here, we argue the most useful aspect of the extended model lies in it's 'off-axis' improvements: Bu can stray further from ϵ at fixed ϵ. Referring back to figure 3, the next-order WDR model captures more of the dynamics sampled by a spectrum of waves (a range of Bu_n) at a given ϵ. Consistent with this goal, we want to keep some correction terms, but we see no reason to use the full expression with the exact choice $Bu = \epsilon$, for which the YBJ equation (3.12) was shown in the previous subsection to match the RSW solutions extremely well. Thus rather than use this equation as derived, we now proceed to consider two subranges.

Consider separately examples for the cases (i) $1 \gg Bu \gg \epsilon$ (e.g. $Bu \sim \epsilon^{1/2}$), (ii) $Bu \sim \epsilon$ and (iii) $\epsilon \gg Bu$ (e.g. $Bu \sim \epsilon^2$). The terms with prefactors in (3.17) then scale as

$$\left.\begin{array}{l} \text{(i)} \ Bu \sim \epsilon^{1/2} : \ \dfrac{Bu}{\epsilon} \sim \epsilon^{-1/2} \gg \dfrac{Bu^2}{\epsilon} \sim 1 \gg Bu \sim \epsilon^{1/2} \gg \epsilon, \\[2mm] \text{(ii)} \ Bu \sim \epsilon : \ \dfrac{Bu}{\epsilon} \sim 1 \gg \dfrac{Bu^2}{\epsilon} \sim Bu \sim \epsilon, \\[2mm] \text{(iii)} \ Bu \sim \epsilon^2 : \ \dfrac{Bu}{\epsilon} \sim \epsilon \gg Bu \sim \epsilon^2 \gg \dfrac{Bu^2}{\epsilon} \sim \epsilon^3. \end{array}\right\} \tag{3.19}$$

In case (i), the new Bu^2/ϵ term is $O(1)$ and the Bu/ϵ term (part of the original YBJ equation) is dominant. The other two terms, both new, are negligible. In case (ii), the three new terms, including $Bu\,G$, are all $O(\epsilon)$ and small compared to the $O(1)$ original term Bu/ϵ. As mentioned above, there is little reason to retain these terms since the original WDR equation was already shown to be accurate. Finally, in case (iii), all terms are small, but the new term, with prefactor ϵ in (3.17), is of the same order as the original term Bu/ϵ, and so should be retained. Below we consider cases (i) and (iii) explicitly.

3.2.1. *Intermediate dispersion regime:* $Bu \sim \sqrt{\epsilon}$

Recall from figure 1 that the modal Burger number decreases monotonically as the mode n increases. For sufficiently small ϵ, some modal Burger numbers satisfy $\epsilon \ll Bu_n \ll 1$, and the number of modes satisfying this scaling increases with decreasing ϵ. This motivates the scaling $Bu \sim \sqrt{\epsilon}$, which we term the 'intermediate dispersion regime'. In this limit, the pressure gradient term in (1.6a) is small, and so does not appear at leading order, but is larger than the mean flow interaction terms. We set $Bu \sim \sqrt{\epsilon}$, set $T = \epsilon t$ and retain terms up to $O(\epsilon)$ in (3.17) to get the 'intermediate dispersion regime' (IDR) amplitude equation

$$\frac{\partial A}{\partial t} + \epsilon J(\Psi, A) + \epsilon \frac{\mathrm{i}}{2}(\Delta\Psi)A - Bu\frac{\mathrm{i}}{2}\Delta A - Bu^2\frac{\mathrm{i}}{8}\Delta^2 A = 0. \tag{3.20}$$

Alternatively, we could have obtained the above amplitude equation by beginning with the scaling $Bu \sim \sqrt{\epsilon}$ in RSW and using multiscale asymptotic analysis as before with $\sqrt{\epsilon}$ as the small parameter. Note that the above equation has two dispersive terms: the higher-order dispersive term, $\Delta^2 A$, which is of the same order as the advection and refraction terms (since $Bu \sim \sqrt{\epsilon}$), is asymptotically smaller than the lower-order dispersive term, ΔA, but is expected to be an important correction on $1/\epsilon$ time scales.

If we ignore the mean flow terms, the dispersion relationship for the above equation has the form $\omega_{idr} = (Bu/2)|\boldsymbol{k}|^2 - (Bu^2/8)|\boldsymbol{k}|^4$. Further if we Taylor expand the dispersion relationship of gravity waves assuming small Burger number, we obtain

$$\sqrt{1 + Bu|\boldsymbol{k}|^2} \sim 1 + \frac{Bu}{2}|\boldsymbol{k}|^2 - \frac{Bu^2}{8}|\boldsymbol{k}|^4. \tag{3.21}$$

Note that the '1' above is associated with the pure inertial frequency part, which was removed by deriving the slowly evolving amplitude equation. Therefore, the higher-order dispersion term in (3.20) corresponds to the dispersive term expected according to the gravity wave dispersion relationship.

To see the improvement obtained by the addition of the higher-order dispersion term in IDR, we set $\epsilon = 0.0125$ and $Bu = \sqrt{\epsilon}$ and compute numerical solutions of the IDR

amplitude equation (3.20), the YBJ equation (3.12) and RSW (3.1). We define the error relative to RSW as

$$e_{idr} = \frac{\left\langle |A_{idr} - A_{rsw}|^2 \right\rangle}{\left\langle |A_{rsw}|^2 \right\rangle}, \tag{3.22}$$

where $\langle \rangle$ denotes spatial averaging, $A_{rsw} = \sqrt{u^2 + v^2}$ is obtained from the numerical solution of (3.1) and A_{idr} is the wave amplitude obtained from the numerical solution of (3.20). Replacing '*idr*' with '*ybj*' indicates the equivalent error for the YBJ equation (3.12) relative to RSW. The results are given in figure 5, panel (*a*) of which shows the amplitude modulus $|A| = \sqrt{u^2 + v^2}$ for IDR, YBJ and RSW at $\epsilon t = 6.25$.

Figure 5(*b*) shows the (root mean square) r.m.s. velocity in the top right quarter of the domain while figure 5(*c*) shows the phase of the wave field calculated based on the average velocities in the top right quarter of the domain. We find that although the magnitudes of the velocity predicted by IDR and YBJ equations are comparable, as can be inferred from figure 5(*b*), the YBJ solution becomes out of phase with RSW solution, the difference increasing with time. This is clearly seen figure 5(*c*) that shows the phase. Observe that for small times, all three models agree in phase and are indistinguishable. However, on longer time scales the YBJ equation deviates significantly from the RSW solution while the IDR solution diverges only slightly. At slow time $T = \epsilon t = 6.25$, when YBJ and RSW are almost completely out of phase, figure 5(*a*) shows the horizontal structure of the velocity field. Observe that while RSW predicts a wave field with increased concentration in anticyclones and decreased concentration in cyclones, a behaviour that is well captured by the IDR equation, the YBJ equation predicts an almost homogeneous wave field at this time. Finally the last panel shows the r.m.s. error between YBJ and IDR equations as compared with RSW. As can be seen, the error of the YBJ equation increases at a much more rapid rate than that for the IDR equation.

3.2.2. *Very weak dispersion regime: Bu $\sim \epsilon^2$*

We now consider very high baroclinic modes, in a regime characterized by $Bu \sim \epsilon^2$. Wave dispersion in this regime is smaller than the mean flow interaction terms and we therefore call this the 'very weak dispersion regime'. Setting $Bu \sim \epsilon^2$ and retaining terms up to $O(\epsilon^2)$ in (3.17), we obtain the vWDR amplitude equation

$$\frac{\partial A}{\partial t} + \epsilon J(\Psi, A) + \epsilon \frac{i}{2}(\Delta\Psi)A - Bu\frac{i}{2}\Delta A - \epsilon^2 \ \frac{i}{8}|\Delta^\perp\Psi|^2 A = 0. \tag{3.23}$$

As in IDR, we note that rather than considering a limiting form of (3.17) we could have obtained the above equation starting from RSW by setting $Bu \sim \epsilon^2$. If we ignore the dispersive and advective terms, we observe that the solution of the amplitude equation may be written as

$$A = A(t=0) \exp\left\{ -it\left(\frac{\epsilon}{2}\Delta\Psi - \frac{\epsilon^2}{8}\sigma^2 \right) \right\}, \tag{3.24}$$

which indicates that the geostrophic vorticity and shear, σ (see (3.5)), shift the frequency of the wave field. Previous works have identified this by simply ignoring the pressure gradient term in RSW right from the start and calculating the frequency shift produced by a mean flow, two notable ones being Fomin (1973) and Chavanne,
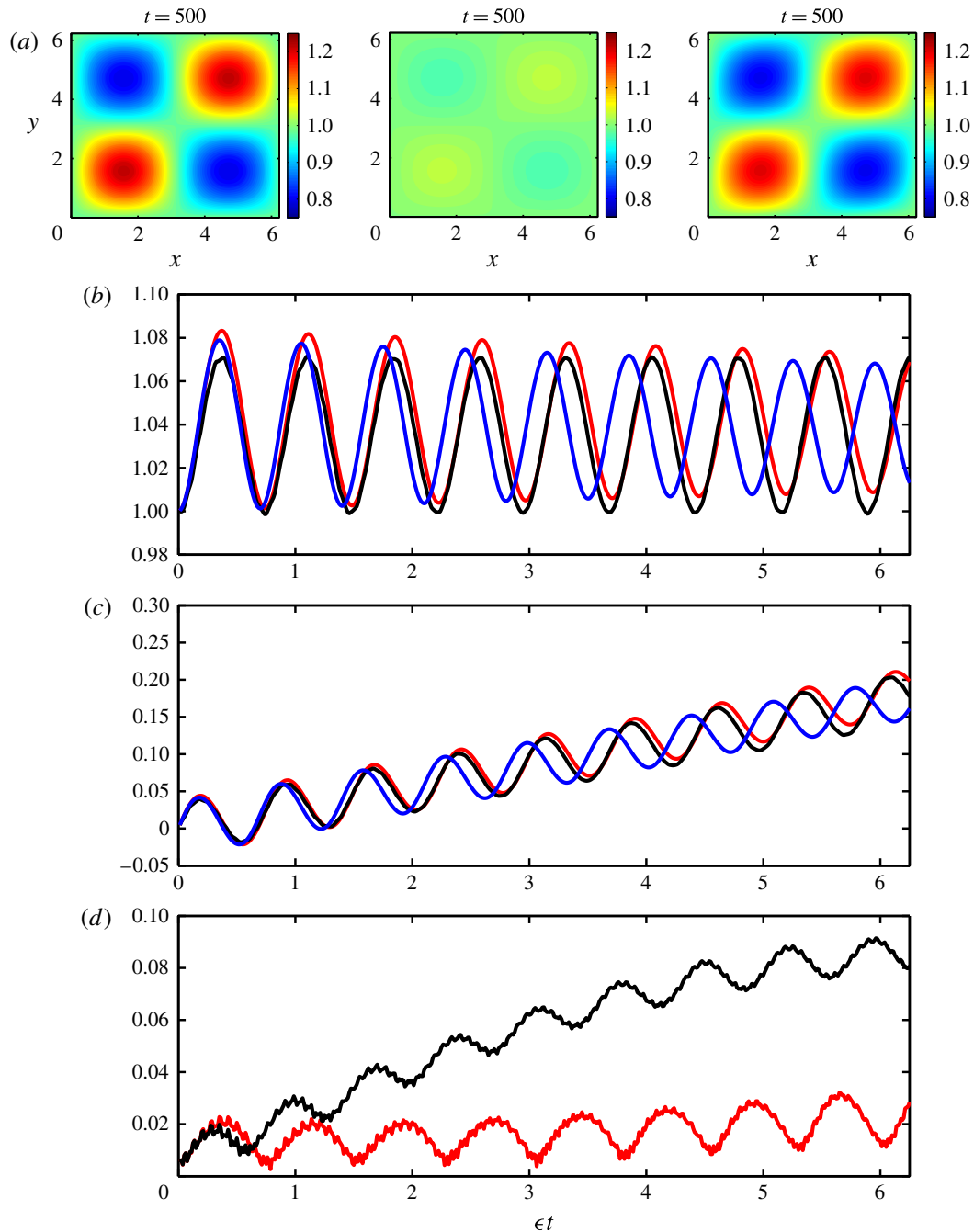
FIGURE 5. (Colour online) (*a*) $|A| = \sqrt{u^2 + v^2}$ for IDR, YBJ and RSW at $\epsilon t = 6.25$. (*b*) $\sqrt{\langle |A|^2 \rangle^{part}}$ (spatial average over top right quarter) obtained from RSW (black), YBJ (blue) and IDR (red). (*c*) Phase (θ, calculated as $\langle A \rangle^{part} = Re^{i\theta}$) of various models with the same colour pattern as the second panel. (*d*) Errors e_{idr} (red curve, see (3.22)) and e_{ybj} (black curve). All the simulations used the parameters $Bu = \sqrt{\epsilon}$, $\epsilon = 0.0125$.

Firing & Ascani (2012). Chavanne *et al.* (2012) finds an expression for effective frequency due to the modulation by a mean flow as (equation (A 5) there):

$$\frac{f_{eff}}{f} = \left\{ 1 + \epsilon \Delta \Psi + \frac{\epsilon^2}{4} \left(\Delta \Psi - \sigma^2 \right) \right\}^{1/2} \sim 1 + \frac{\epsilon}{2} \Delta \Psi - \frac{\epsilon^2}{8} \sigma^2 + O(\epsilon^3), \quad (3.25)$$

which after removing the '1' agrees with our expression in (3.24). The vWDR amplitude equation (3.23) therefore captures the next-order refraction term due to geostrophic shear in addition to the contribution from vorticity.

Since the wave dispersion is very weak in this regime, evolution of the wave field is even slower than for the other regimes. We therefore choose a higher Rossby number, $\epsilon = 0.125$, to facilitate long-time simulations. We now compare the vWDR and YBJ amplitude equations with RSW. Figure 6(*a*) compares the spatial structure of $|A|$ obtained from these three models. Figure 6(*b*,*c*) shows the r.m.s. and phase of the wave field in the top right quarter of the domain, while figure 6(*d*) shows the r.m.s. error between the vWDR and YBJ equations relative to RSW. Overall we find two important results. First, the vWDR is characterized by smaller wave field features in comparison with the other two cases considered so far. The formation of small-scale features in the wave field results in deviations between the reduced models and RSW, the difference increasing with time. Although all three models agree for an initial period, the magnitude and phase of the reduced models deviate from the parent model. Second, we note that the higher-order refraction term that forms a correction term to YBJ in this regime does not improve the features of the YBJ model. While not apparent here, in the next section we show that, with or without this term, the amplitude equation breaks down faster than expected; scaling of the conservation law for the amplitude equation offers an explanation.

3.3. *The strong dispersion regime*

Recall that low baroclinic modes may have $Bu \sim O(1)$, explicitly violating the initial assumption of YBJ that the Burger and Rossby numbers are of the same order. Because there can be no resonant forcing of the leading-order equation in this case, low baroclinic modes remain unmodulated for time scales $t \sim 1/\epsilon$. However, as we show, resonant modulation of the NIWs is possible at time scales $t \sim 1/\epsilon^2$. We therefore define a slow time scale $T = \epsilon^2 t$ and set $\partial/\partial t \to \partial/\partial t + \epsilon^2 \partial/\partial T$ to rewrite (3.1) as

$$\frac{\partial \boldsymbol{v}}{\partial t} + \hat{\boldsymbol{z}} \times \boldsymbol{v} + Bu\nabla p + \epsilon \{\boldsymbol{v} \cdot \nabla \boldsymbol{V} + \boldsymbol{V} \cdot \nabla \boldsymbol{v}\} + \epsilon^2 \frac{\partial \boldsymbol{v}}{\partial T} = 0, \qquad (3.26a)$$

$$\frac{\partial p}{\partial t} + \nabla \cdot \boldsymbol{v} + \epsilon\ \boldsymbol{V} \cdot \nabla p + \epsilon^2 \frac{\partial p}{\partial T} = 0. \qquad (3.26b)$$

We now expand all variables as an asymptotic series in ϵ, with the notation

$$(\boldsymbol{v}, p) = (\boldsymbol{v}_0, p_0) + \epsilon(\boldsymbol{v}_1, p_1) + O(\epsilon^2). \qquad (3.27)$$

At $O(1)$, (3.26) become

$$\frac{\partial \boldsymbol{v}_0}{\partial t} + \hat{\boldsymbol{z}} \times \boldsymbol{v}_0 + Bu\nabla p_0 = 0, \qquad (3.28a)$$

$$\frac{\partial p_0}{\partial t} + \nabla \cdot \boldsymbol{v}_0 = 0. \qquad (3.28b)$$

These are the standard linear equations for inertia–gravity waves. For the initial conditions (3.2*a*,*b*), consisting of a horizontally uniform inertial wave field, the
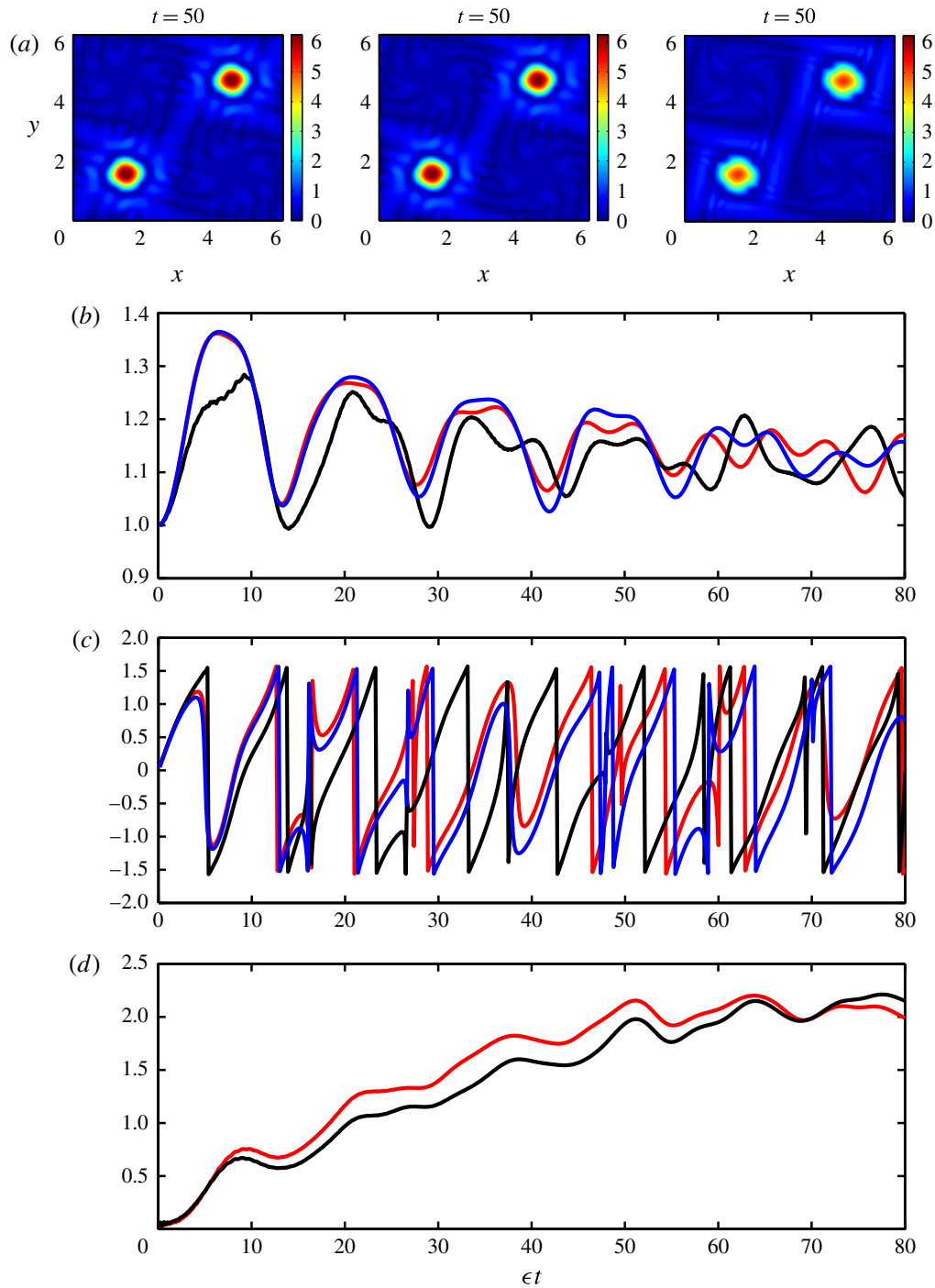
FIGURE 6. (Colour online) (a) $|A| = \sqrt{u^2 + v^2}$ for vWDR, YBJ and RSW at $\epsilon t = 6.25$. (b) $\sqrt{\langle |A|^2 \rangle^{part}}$ obtained from RSW (black), YBJ (blue) and vWDR (red). (c) Phase (θ, calculated as $\langle A \rangle^{part} = R e^{i\theta}$) of various models with the same colour pattern as (b). (d) Errors e_{vwdr} (red curve) and e_{ybj} (black curve). All the simulations used the parameters $Bu = \epsilon^2, \epsilon = 0.125$.

solution to (3.28) remains horizontally uniform and is given by

$$\boldsymbol{v}_0 = \tfrac{1}{2} A(T)(\hat{\boldsymbol{x}} - \mathrm{i}\hat{\boldsymbol{y}})\mathrm{e}^{-\mathrm{i}t} + \text{c.c.} \quad \text{and} \quad p_0 = 0. \qquad (3.29a,b)$$

Notice that the wave amplitude A is expected to evolve in the slow time T.

At $O(\epsilon)$, equations (3.26) lead to

$$\frac{\partial \boldsymbol{v}_1}{\partial t} + \hat{\boldsymbol{z}} \times \boldsymbol{v}_1 + Bu\nabla p_1 = -\boldsymbol{v}_0 \cdot \nabla V, \qquad (3.30a)$$

$$\frac{\partial p_1}{\partial t} + \nabla \cdot \boldsymbol{v}_1 = 0. \qquad (3.30b)$$

Using the result in appendix B, the above equations can be transformed to obtain

$$\mathscr{L} \boldsymbol{v}_1 = \Delta \left\{ -\Psi \frac{\partial \boldsymbol{v}_0}{\partial t} + Bu\boldsymbol{v}_0 \cdot \nabla V \right\}, \qquad (3.31a)$$

$$\mathscr{L} p_1 = \Delta \left\{ Bu\boldsymbol{v}_0 \cdot \nabla \Psi \right\}, \qquad (3.31b)$$

where

$$\mathscr{L} = \frac{\partial}{\partial t} \left(\frac{\partial^2}{\partial t^2} + 1 - Bu\Delta \right). \qquad (3.32)$$

These equations may be considered a diagonalized form of (3.30). The solution of the above system consists of a particular solution of inertial frequency and a homogeneous solution consisting of gravity waves and a steady part (see for example Danioux & Klein 2008). The particular solution of inertial frequency may be obtained from the above equations by observing that $\boldsymbol{v}_0$ has no spatial dependence and satisfies $(\partial^2/\partial t^2 + 1)\boldsymbol{v}_0 = 0$. The solution of above system may be expressed as

$$\boldsymbol{v}_1 = \frac{1}{Bu}\Psi \boldsymbol{v}_0 + \frac{\partial \boldsymbol{v}_0}{\partial t} \cdot \nabla V + \boldsymbol{v}^h, \qquad (3.33a)$$

$$p_1 = \frac{1}{Bu}\frac{\partial \boldsymbol{v}_0}{\partial t} \cdot \nabla \Psi + p^h, \qquad (3.33b)$$

where the superscript 'h' denotes homogeneous solution of (3.30). Reverting again to complex velocity notation, $\mathscr{U} = u + iv$, for the horizontal velocity modes, we use (3.33a) to obtain $\mathscr{U}_1 = \mathscr{U}_1^{io} + \mathscr{U}_1^h$, where $\mathscr{U}_1^{io}$ and $\mathscr{U}_1^h$ represent the particular solution (inertial waves) and the homogeneous solution at $O(\epsilon)$, respectively, with

$$\mathscr{U}_1^{io} = \left(\frac{1}{Bu}\Psi + \frac{1}{2}\Delta\Psi \right) A e^{-it} + \frac{1}{2} \left(\Delta^\perp \Psi \right) A^* e^{it}. \qquad (3.34)$$

An expression for $\mathscr{U}_1^h$ for arbitrary Ψ may be written in terms of a Green's function or Fourier modes. However, this is not attempted here since we require only the general expression for the inertial wave part to calculate the modulation of the leading inertial wave field in SDR for $t \sim 1/\epsilon^2$; the homogeneous part does not resonantly force the inertial frequency and therefore cannot modulate the leading-order inertial wave field. We note that although the leading-order inertial wave field is not affected by the mean flow for time scales $t \sim 1/\epsilon$, the interaction leads to the formation of weak $O(\epsilon)$ inertial wave fields, as seen in (3.34).

To capture the modulation of inertial waves by the balanced flow in the long-time limit, $t \sim 1/\epsilon^2$, we proceed to $O(\epsilon^2)$. The momentum equation (3.26a) at this order is

$$\frac{\partial \boldsymbol{v}_2}{\partial t} + \hat{\boldsymbol{z}} \times \boldsymbol{v}_2 + Bu\nabla p_2 = -\left(\frac{\partial \boldsymbol{v}_0}{\partial T} + \boldsymbol{v}_1 \cdot \nabla V + V \cdot \nabla \boldsymbol{v}_1 \right) \qquad (3.35)$$

or, in terms of the complex velocity,

$$\frac{\partial \mathcal{U}_2}{\partial t} + i\mathcal{U}_2 + Bu\left(\frac{\partial}{\partial x} + i\frac{\partial}{\partial y}\right)p_2 = -\left(\frac{\partial \mathcal{U}_0}{\partial T} + \mathcal{R}\right), \quad (3.36)$$

where

$$\mathcal{R} = \nabla \cdot (\mathcal{U}_1 V) + \frac{i}{2}\left(\mathcal{U}_1 \, \Delta \Psi + \mathcal{U}_1^* \Delta^\perp \Psi\right). \quad (3.37)$$

The left-hand side of equation (3.36) supports the whole spectrum of gravity waves. To obtain the amplitude equation for NIWs using a solvability condition, we spatially average (3.36) and use (3.34) to obtain

$$\frac{d\langle \mathcal{U}_2 \rangle}{dt} + i\langle \mathcal{U}_2 \rangle = -\left(\frac{d\mathcal{U}_0}{dT} + \langle \mathcal{R} \rangle\right), \quad (3.38)$$

where $\langle \rangle$ refers to spatial averaging over the whole domain and

$$\langle \mathcal{R} \rangle = \frac{i}{4}\left\langle \left(\frac{2\Psi}{Bu} + \Delta \Psi\right)\Delta \Psi - \Delta^\perp \Psi \Delta^{\perp *}\Psi \right\rangle Ae^{-it} + \text{NR} \quad (3.39)$$

$$= -\frac{i}{2Bu}\langle(\nabla \Psi)^2\rangle Ae^{-it} + \text{NR}. \quad (3.40)$$

Non-resonant (NR) terms consist of factors multiplying e^{it} and the homogeneous solution. The second line follows from multiple applications of integration by parts (for example, $\langle \Psi_{xy}^2 \rangle = \langle \Psi_{xx}\Psi_{yy} \rangle$, with subscripts indicating partial derivatives) and some simplification, which ensures that all the terms except $\langle \Psi \Delta \Psi \rangle$ cancel.

The solvability condition now consists of setting the terms containing e^{-it} on the right-hand side of (3.38) to zero. This gives the amplitude equation

$$\frac{dA}{dT} - \frac{i}{2Bu}\langle(\nabla \Psi)^2\rangle \, A = 0 \quad (3.41)$$

whose solution may be written as

$$A(T) = A(0)\exp\left[\frac{\langle(\nabla \Psi)^2\rangle}{2Bu}iT\right]. \quad (3.42)$$

Thus the horizontally averaged kinetic energy of the balanced flow lowers the frequency of the NIWs from the initial inertial frequency, making them subinertial. Since different baroclinic modes have different Bu, this can lead to vertical dispersion of the modes in SDR in the long-time limit. We compare this asymptotic prediction by numerically integrating (3.1) with $Bu = 1$ and $\epsilon = 0.125$ (since in SDR, we will need to numerically integrate for times of order $t \sim 1/\epsilon^2$, we chose the higher Rossby number). Figure 7 shows comparisons between the asymptotic prediction and numerical solution of RSW and it is seen that the difference is negligible for the time scales considered.
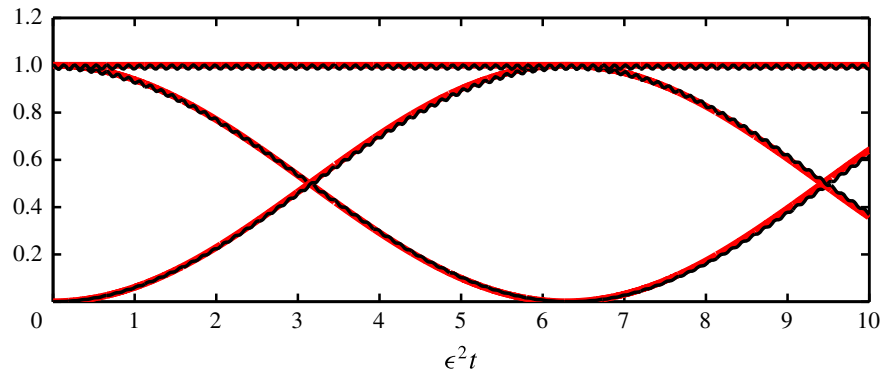
FIGURE 7. (Colour online) Comparison between asymptotic prediction for SDR (3.42) (red curve) and numerical solution of RSW (3.1) (black curve) for $\epsilon = 0.125$ and $Bu = 1$. The straight line is $\langle u \rangle^2 + \langle v \rangle^2$, the curve beginning at 1 is $\langle u \rangle^2$ and the curve beginning at 0 is $\langle v \rangle^2$. Observe that the black curves lie over the red curves indicating the exceptional agreement between the asymptotic predictions and numerical results.

A note on the 'strong dispersion approximation' of YBJ

Section 5 of YBJ introduces a further approximation to their amplitude equation based on a spatial scale separation between NIWs and the background flow. Defining μ as the ratio of eddy horizontal scales to wave horizontal scales (equation (5.2) in YBJ), they refer to the limit $\mu \ll 1$ as the 'strong dispersion approximation' (SDA). Further, since SDA uses only the YBJ equation, ignoring the $O(\epsilon)$ corrections to the leading-order wave field (expressed in equation (2.25) in YBJ), one requires $\mu \gg \epsilon$ and therefore one has the ordering of small parameters: $\epsilon \ll \mu \ll 1$. The asymptotic expansion of the velocity field for example may be rewritten as $\mathcal{U} = A_{00}(t) + \mu A_{01}(x, y, t) + O(\max(\mu^2, \epsilon))$, where A_{00} and A_{01} are asymptotic expansions of the leading-order NIWs amplitude A_0, as seen in (3.10a,b) (these are expressed as $\bar{A}$ and A', respectively, in YBJ – see their equation (5.6)). Asymptotic expansions in μ may be used to obtain expressions for A_{01} (equation (5.12) in YBJ), which is the leading-order spatially inhomogeneous wave field (since A_{00} is spatially homogeneous). YBJ use this result to argue that NIWs in the SDA must concentrate in anticyclones.

In contrast the leading-order wave field in SDR is homogeneous with infinite horizontal scales, implying that $\mu \to \infty$, and the next-order inhomogeneities are $O(\epsilon)$ with spatial scales of the order of the mean flow scales. These $O(\epsilon)$ inhomogeneous fields consist of pure inertial oscillations and gravity waves of varying frequencies, as indicated in (3.33a). Since the leading inhomogeneous field in SDA is different from that in SDR, the predictions of anticyclonic trapping using the YBJ equation do not apply in SDR. This is in spite of the fact that both SDA and SDR predict the same equation for the leading-order homogeneous wave field: the SDR amplitude equation, (3.41) is identical to the SDA leading-order amplitude equation for A_{00} (equation (5.10) in YBJ), despite that the procedure followed in deriving them are completely different.

Therefore in SDR there is no affinity of NIWs towards anticyclones, while SDA predicts the opposite. Note that since SDA uses the YBJ equation as its parent model, the solution of the YBJ equation captures all the asymptotic results obtained with μ as the small parameter. To illustrate that SDA is not valid in SDR, we integrate RSW and the YBJ equation by setting $Bu = 1$ in both models; the results are shown in
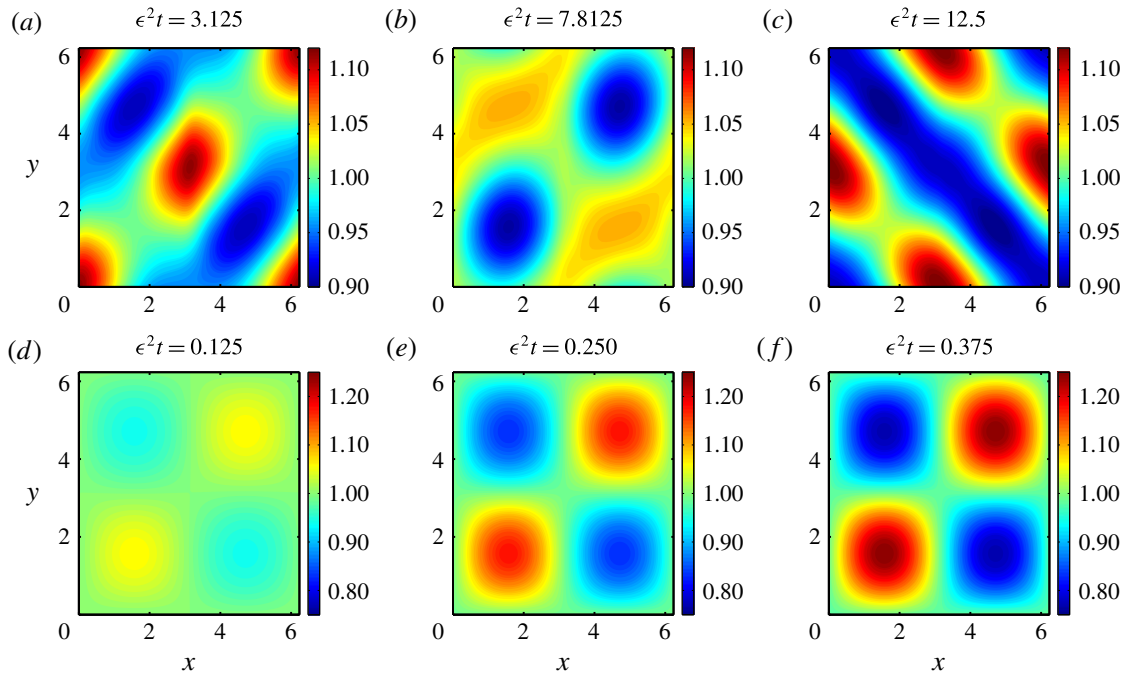
FIGURE 8. (Colour online) (*a–c*) and (*d–f*) show $|A|$ from the RSW and YBJ simulations, respectively. Both simulations used $Bu = 1$ and $\epsilon = 0.125$. The solution of RSW in SDR fluctuates on a fast time scale due to the excitation of non-inertial gravity waves, as expressed in (3.33*a*). The RSW solution is in general therefore very different from what may be obtained by integrating the YBJ in SDR, or based on the strong dispersion approximation on the YBJ equation, the latter being a subset of the solution of the YBJ equation. A noticeable difference is the trapping of waves in anticyclones in the YBJ case (as predicted), a feature that is not seen in the parent model, RSW even after long times.

figure 8. The RSW solution consists of fast wave fields consisting of gravity waves and inertial waves (see (3.33)) in addition to spatially homogeneous inertial waves and, even after long times, shows no affinity towards anticyclones. In contrast, the YBJ equation integrated with the same parameters shows a tendency for the wave field to concentrate in anticyclones. This experiment indicates that the YBJ equation cannot capture the features of the SDR; therefore SDA, which is a further reduction of the YBJ equation, does not hold in the SDR.

4. Conservation laws, trapping of NIWs in anticyclones and small-scale formation in the weak dispersion regimes

In this section, we identify conservation laws for the weak dispersion amplitude equations, and in this context consider the trapping of NIWs in anticyclones and scaling arguments for breakdown of the amplitude equations in vWDR. We first note that the YBJ equation has two conservation laws (Danioux, Vanneste & Bühler 2015, hereafter DVB). The first is

$$\frac{\mathrm{d}}{\mathrm{d}t}\langle |A|^2 \rangle = 0, \tag{4.1}$$

where angle brackets denote spatial averaging; it follows from $\langle A^*(3.12) + \mathrm{c.c.} \rangle$ (where the 0 subscript has been dropped). This conservation law is due to the symmetry

associated with translational invariance of the phase of NIWs, i.e. $A \rightarrow A \mathrm{e}^{\mathrm{i}s}$, and therefore may be called the 'action' integral (Xie & Vanneste 2015). Note that action is also proportional to the kinetic energy of the waves ($|A|^2 = u^2 + v^2$) and therefore NIWs cannot exchange kinetic energy with the mean flow. The second invariant is

$$\frac{\mathrm{d}}{\mathrm{d}t} \mathscr{E}_{ybj} = 0, \quad \mathscr{E}_{ybj} = E_{adv} + E_{disp} + E_{refr}, \quad (4.2a,b)$$

$$E_{adv} = \mathrm{i}\epsilon \left\langle \Psi J(A^*, A) \right\rangle, \quad E_{disp} = \frac{Bu}{2} \left\langle |\nabla A|^2 \right\rangle, \quad E_{refr} = \frac{\epsilon}{2} \left\langle (\Delta \Psi) |A|^2 \right\rangle. \quad (4.3a-c)$$

This follows from computing $\langle \mathrm{i} \partial A^* / \partial t \, (3.12) + \mathrm{c.c.} \rangle$, and arises due to the time translational symmetry (consistent with the requirement of a steady mean flow) and thus may be interpreted as the 'energy' (however, note that this is not the physical energy – kinetic, potential or sum – of the waves). While a steady mean flow is required to obtain this conservation law, the asymptotic derivation of the amplitude equation may be extended for the case of a mean flow that evolves on the slow time scale, ϵt.

It then follows that the potential energy of the wave field (proportional to $|\nabla A|^2$) is not conserved, unlike kinetic energy, and thus may be exchanged with the mean flow. As was pointed out by Xie & Vanneste (2015), this is a mechanism by which the waves can extract energy from the mean flow: modulation of the waves by the mean flow leads to smaller wave scales, and hence an increase in the potential energy of the waves, potentially providing a sink for the energy of mesoscale eddies. Although Xie & Vanneste (2015) considered a parameter regime where the waves are stronger than the mean flow, due to the absence of resonant nonlinear terms, the wave evolution equation is exactly same as the basic YBJ equation (lack of nonlinear wave interaction terms for NIWs is due to the absence of resonant wave triads or quartics between pure inertial frequency components, see for example Wagner & Young 2016 and Zeitlin, Reznik & Ben Jelloul 2003). In the regime studied here, where the waves are weaker than the mean flow, the same mechanism is at play, but the energy extracted by the waves from the mean flow is asymptotically smaller than the total mean flow energy. This is also why the assumption of a steady mean flow is consistent in this study.

The IDR and vWDR equations have similar conservation laws and can be derived following the same procedure above. The first conservation law, action, remains the same for IDR and vWDR equations. The 'energy' conservation laws for IDR and vWDR equations are, respectively,

$$\frac{\mathrm{d}}{\mathrm{d}t} \mathscr{E}_{idr} = 0, \quad \mathscr{E}_{idr} = \mathscr{E}_{ybj} + E_{disp2}, \quad E_{disp2} = -\frac{Bu^2}{8} \left\langle |\Delta A|^2 \right\rangle \quad (4.4a-c)$$

and

$$\frac{\mathrm{d}}{\mathrm{d}t} \mathscr{E}_{vwdr} = 0, \quad \mathscr{E}_{vwdr} = \mathscr{E}_{ybj} + E_{refr2}, \quad E_{refr2} = -\frac{\epsilon^2}{8} \left\langle |\Delta^\perp \Psi|^2 |A|^2 \right\rangle. \quad (4.5a-c)$$

Following DVB, one may use scaling arguments applied to these conservation laws to understand why wave activity increases in anticyclones. Because the IDR and vWDR equations are basically the YBJ equation with correction terms that matter at long times, these arguments are a trivial extension of DVB and are not repeated here.
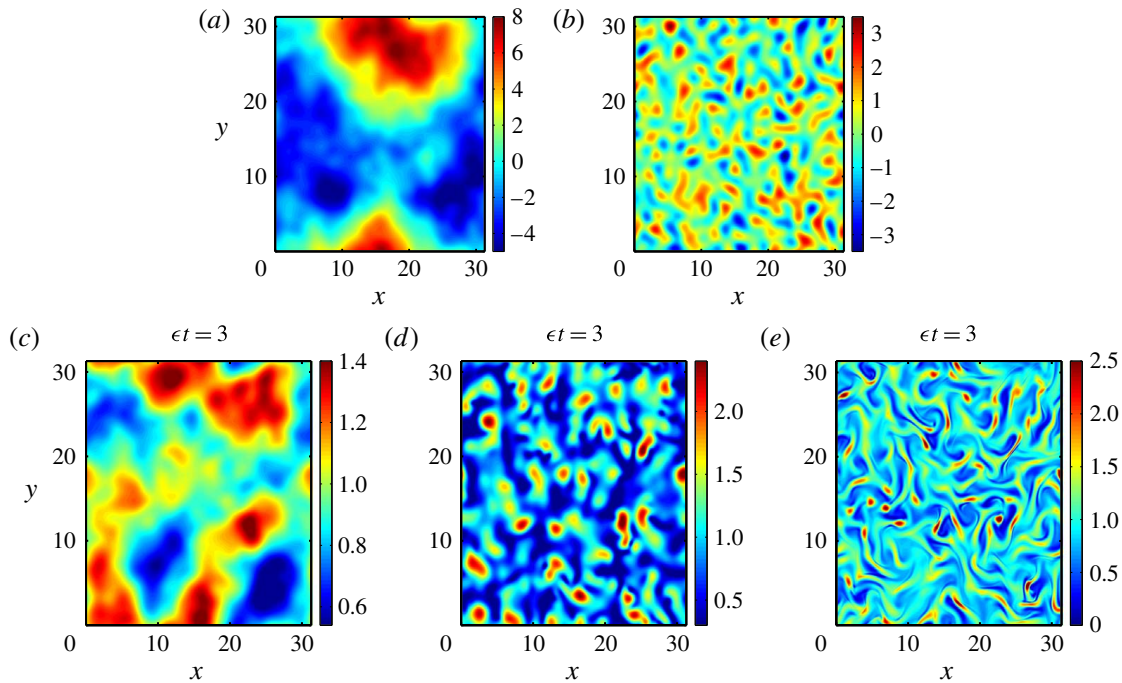
FIGURE 9. (Colour online) (*a*) Streamfunction and (*b*) associated vorticity. (*c–e*) Amplitude modulus $|A|$ obtained from numerical solutions of RSW: (*c*) IDR ($\epsilon = 0.0125$ and $Bu = \sqrt{\epsilon}$); (*d*) YBJ ($\epsilon = Bu = 0.0125$); (*e*) vWDR ($\epsilon = 0.125$ and $Bu = \epsilon^2$).

We instead consider these conservation terms in the context of additional numerical simulations. For completeness we use a somewhat more natural mean flow field, obtained by numerically integrating the two-dimensional vorticity equation initialized with uniformly distributed random numbers in the interval $(0, 10)$ on the grid points. The size of the domain was increased to $[0,\ 10\pi] \times [0,\ 10\pi]$ and the time integration was stopped when the vortical fields that formed had spatial scales approximately one-tenth of the domain size, so that in non-dimensional form the vortical structures of the mean flow have $O(1)$ length scales. We further scaled the r.m.s. vorticity such that $\langle (\Delta \Psi)^2 \rangle = 1$. The vorticity field and the corresponding streamfunction are shown in figure 9(*a,b*).

Figure 9(*c–e*) shows the amplitude modulus $|A|$ in three cases: IDR ($\epsilon = 0.0125$, $Bu = \sqrt{\epsilon}$), YBJ ($\epsilon = Bu = 0.0125$) and vWDR ($\epsilon = 0.125$, $Bu = \epsilon^2$), by integrating the RSW equations using this non-evolving mean flow, and initialized with a homogeneous wave field. Just as in the previous section, the solutions of each amplitude equation provide faithful approximations to the RSW solutions (figures not shown, but see figure 10), although we found that in the very weak dispersion regime, on longer time scales, the solution of the vWDR amplitude equation deviates from the RSW solution due to the formation of smaller spatial scales (discussed below).

Figure 10 shows time series of the energy terms in (4.2)–(4.5). Overall, the energy terms from the amplitude equations and RSW are strikingly similar. A variable that measures the correlation between anticyclonic vorticity and wave strength is E_{refr} in (4.2); note that it is negative in all cases, consistent with anticyclonic trapping in the limit $Bu \ll 1$. Figure 10(*a,b*) shows results from the IDR. One can see that the refraction term balances the lower-order dispersion terms. Assuming the spatial scale of waves to be l, we note that $l \gg 1$ and $l \ll 1$ means the wave field has larger
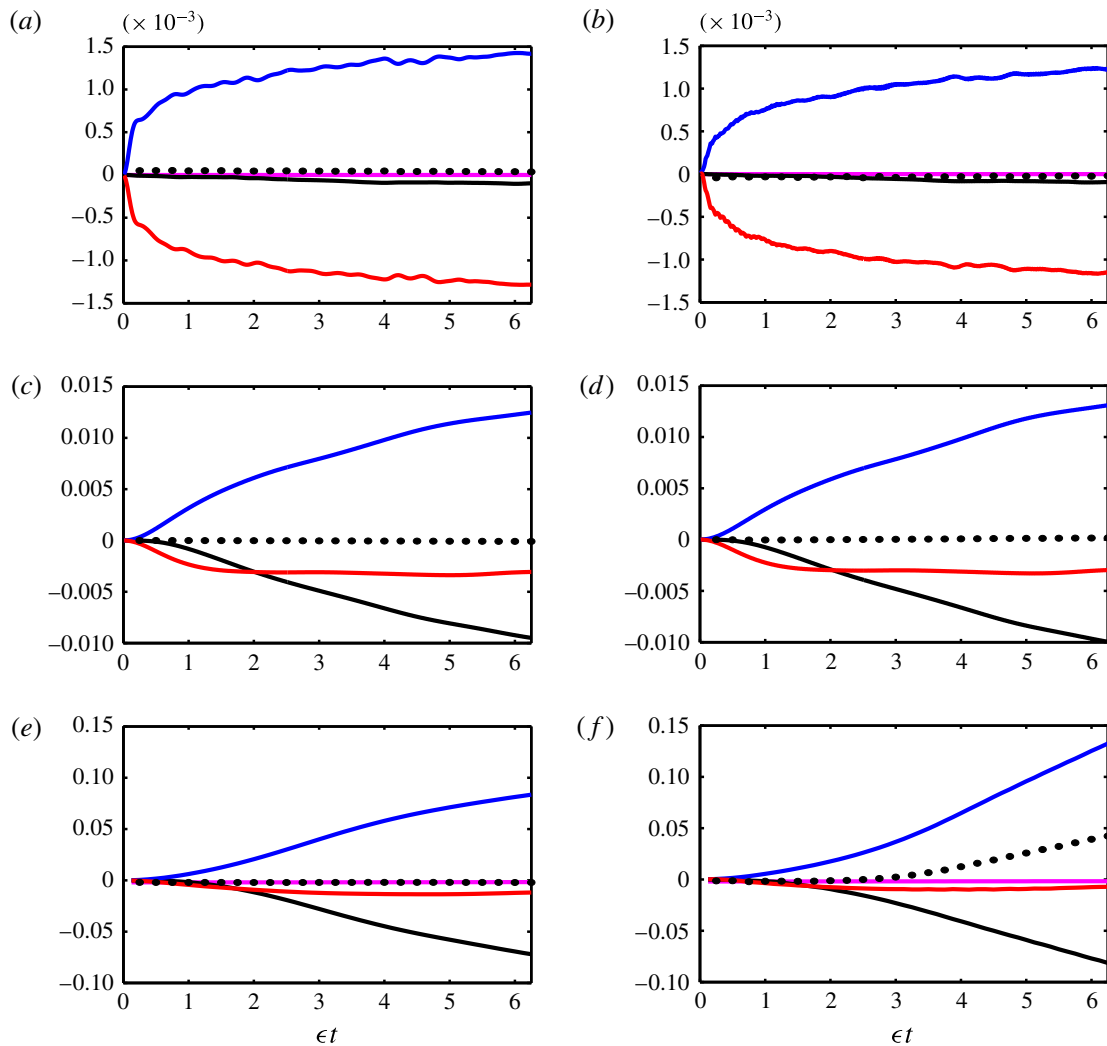
FIGURE 10. (Colour online) Components of the energy terms in the conservation laws for the amplitude equations (4.4) for IDR (a,b), (4.2) for YBJ (c,d) and (4.5) for vWDR (e,f). (a,c,f) Show results from the respective amplitude equations, and (b,d,f) show the same terms computed from the RSW solution. In (a,b) for IDR, the curves are E_{adv} (black curve), E_{disp} (blue curve), E_{refr} (red curve), E_{disp2} (magenta curve) and $\mathscr{E}_{idr}$ (discontinuous black curve), as functions of the slow time ϵt, for $\epsilon = 0.0125$ and $Bu = \sqrt{\epsilon}$. In (c,d) for YBJ, the curves are E_{adv} (black curve), E_{disp} (blue curve), E_{refr} (red curve) and $\mathscr{E}_{ybj}$ (discontinuous black curve), as functions of the slow time ϵt for $\epsilon = Bu = 0.0125$. In (e,f) for vWDR, the curves are E_{adv} (black curve), E_{disp} (blue curve), E_{refr} (red curve), E_{refr2} (magenta curve) and $\mathscr{E}_{vwdr}$ (discontinuous black curve), as functions of the slow time ϵt for $\epsilon = 0.125$ and $Bu = \epsilon^2$.

or smaller spatial scales than the mean flow, respectively, since the mean flow has $O(1)$ spatial scales in non-dimensional form. If we equate the refraction and dispersion terms, we obtain $l \sim \sqrt{Bu/\epsilon} \gg 1$ as a scaling estimate for the wave field, implying that the spatial scale of the wave field is larger than that of the mean flow in this regime, as also seen in figure 9(c).

   In the vWDR experiment shown in figure 10(e,f), one sees that the total energy $\mathscr{E}_{vwdr}$, although exactly conserved in the amplitude equation, increases with time when
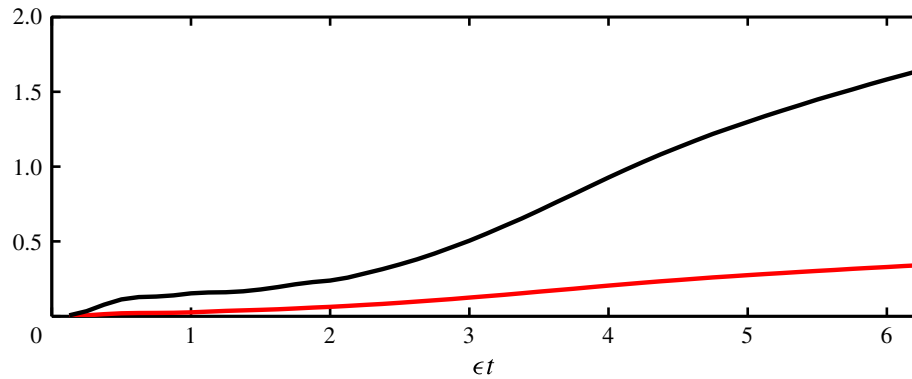
FIGURE 11. (Colour online) $Bu\sqrt{\langle|\nabla p|^2\rangle}$ (red curve) and $\epsilon\sqrt{\langle|\boldsymbol{V}\cdot\nabla p|^2\rangle}$ (black curve) obtained by integrating RSW with the same parameters used for figure 10(*e*,*f*).

calculated using the RSW solution, indicating a breakdown of the assumptions that led to the vWDR amplitude equation. Note that both of the refraction terms are negligible (consistent with results shown in § 3), with instead the advection term balancing the dispersion term. This is a consequence of the small spatial scale formation in the wave field, resulting in amplification of the spatial derivatives of the wave amplitude. These two features are also obvious from figure 9(*e*).

To understand this, consider the following scaling argument. Balancing the dispersive and advection terms, we find $l \sim Bu/\epsilon$ and since $Bu \sim \epsilon^2$ we obtain an estimate for the scales of the wave field as $l \sim \epsilon$. Since the horizontal length of the wave field scales as $l \sim \epsilon$ the advective nonlinearity U/fl, which resembles Rossby number with wavelength scale l replacing mean flow scale L, can reach $O(1)$ values and pressure gradients can increase beyond the scaling assumptions of vWDR. We plot the pressure gradient terms and the largest mean flow interaction terms in figure 11. Observe that the mean flow interaction terms become $O(1)$, invalidating our asymptotic analysis which assumed these terms to be small. Similarly, the pressure gradient term becomes $O(\epsilon)$, since $Bu\nabla p \sim \epsilon^2/l \sim \epsilon$, violating the initial scaling of $O(\epsilon^2)$. However, we note that the wave field is still near inertial, since the pressure gradient term is asymptotically small. The breakdown of the asymptotic model due to the increased magnitude of the mean flow interaction terms imply that the conservation law for the vWDR amplitude equation need not be conserved when calculated using RSW.

We observe that the refraction term is negative definite in IDR and takes very small negative values in vWDR. This term is therefore expected to be negative in the regime $Bu \sim \epsilon$, assuming a smooth change in variables. This is the crux of the argument made in DVB to explain trapping of waves in anticyclones based on the YBJ equation. Further, while IDR and vWDR have, respectively, larger and smaller spatial scales than the mean flow, the $Bu \sim \epsilon$ regime has scales comparable to that of the mean flow, as can be seen in figure 9(*d*). As a consequence, dispersion, refraction and advection terms in the amplitude equation are all non-negligible, as may be inferred from figure 10(*c*,*d*), a feature that is faithfully observed in RSW as well.

In summary, we note three important observations resulting from this section. Scaling arguments applied to the conservation laws, as pointed out by DVB, can be easily modified for the IDR and vWDR equations and therefore the increased wave activity in anticyclones is a generic feature of the weak dispersion regime.

Further, energy components when calculated using RSW solutions agree quite well with the amplitude equation predictions, which again is not an obvious statement for an arbitrary mean flow such as the one we considered. Finally, based on scaling estimates, we find that the vWDR develops small-scale features as a generic property, resulting in $O(1)$ advective nonlinearity, U/fl, for the wave field. This restricts the long-term validity of a reduced model in this regime.

5. Discussion

In this paper we have investigated the resonant modulation of small-amplitude NIWs, initially confined to the mixed layer, by a steady barotropic mean flow. Although this wave-mean flow interaction problem has been considered before, a unified and comprehensive treatment of the different interaction regimes using asymptotic analysis and numerical simulations is a novel feature of this work. As we have shown, the key non-dimensional parameter that determines the nature of the interaction is the Burger number for each baroclinic mode onto which the wave field projects, $Bu_n = (NH/\lambda_n fL)^2$, where H is the depth of the ocean and L represents the eddy horizontal scale. Depending on the relationship between the modal Burger number and the Rossby number of the balanced flow, ϵ, we considered two broad asymptotic regimes – strong and weak dispersion.

The weak dispersion regime characterized by $Bu \ll 1$ can contain significant number of baroclinic modes and several previous works have used the YBJ equation to capture the features of this regime. We derived a next-order YBJ equation to extend the range of validity of the amplitude equation. The extended YBJ equation was applied to two subregimes of WDR – intermediate and very weak dispersion regimes. The intermediate dispersion regime is a stretch towards the limit where Burger number becomes larger than the Rossby number, while remaining asymptotically small. A higher-order dispersion term added to the YBJ equation was seen to be crucial to capture the features of this regime.

The vWDR on the other hand considers the other extreme limit of Burger number being asymptotically smaller than the Rossby number. A higher-order refraction term arises as a correction term to YBJ equation in this regime, but this term is unimportant in simulations. The vWDR equation is an example of an asymptotic model that leads to its own demise: with increasing time the wave field acquires finer scales, leading to the breakdown of the scaling assumptions used to derive it, and thus significant deviations from the parent model. It must however be noted that the reduced model works well in the regime $\epsilon^2 \ll Bu \ll \epsilon$, while the failure associated with vWDR is for $Bu \lesssim \epsilon^2$. From an oceanographic perspective, vWDR can contain significant wave shear and therefore could be important for wave breaking and shear-induced mixing. Of course, a comprehensive modelling of this phenomenon would require taking into account the complete nonlinear dynamics of the interaction problem, neglected in this study.

The other major regime, SDR, is characterized by a homogeneous inertial wave field at leading order, with mean flow kinetic energy modulating the wave field. As we showed using numerical simulations, the wave field inhomogeneities are weak in this regime and the wave does not develop significant features of the mean flow, justifying the separation of this as a completely different regime like the WDR.

It was further seen that increased wave activity in anticyclones is a feature of the WDR and follows directly based on scaling estimates using conservation laws as shown by DVB. Numerical experiments reveal that as Burger number decreases from

$O(1)$ values, the wave field starts trapping in anticyclones and with decreasing Burger number, the scales of the wave field keep decreasing. In IDR and vWDR the scales of the wave field are larger and smaller than the mean flow scales, respectively, with the wave and mean flow scales being comparable in the regime where Burger number is of the same order as Rossby number, where the YBJ equation applies exactly.

Based on our discussion in WDR, we found that the higher-order dispersion term could significantly improve the features of the YBJ equation in IDR while the additional refraction term was seen not to improve the vWDR features. One might therefore consider using the IDR equation, which is essentially YBJ with a higher-order correction term, as an 'improved' YBJ equation to cover a wider range of the weak dispersion regimes. However, this additional correction term, while apparently asymptotically small in the range $Bu \gtrsim O(\epsilon)$, causes problems in the vWDR. As seen in the last section, the small-scale formation that bedevils the vWDR is due to the dispersive term (corresponding to the 'energy' term E_{disp} in (4.2)). The higher-order dispersive term that arises in IDR produces an even faster breakdown of the amplitude equation in the vWDR (we checked this numerically, but omit the relevant figure). This is easily seen based on the scaling estimates presented for vWDR previously. Observe that for $Bu \sim \epsilon^2$ and $l \sim \epsilon$ both dispersive terms in (3.20) becomes comparable, resulting in larger errors on incorporating the higher dispersion term in vWDR.

To summarize, for practical applications, the relevant modal amplitude equations are

$$Bu_n \sim 1: \quad \frac{\partial A_n}{\partial t} - \frac{\mathrm{i}\epsilon^2}{2Bu_n}\langle(\boldsymbol{\nabla}\Psi)^2\rangle A_n = 0, \tag{5.1}$$

$$Bu_n \ll 1: \quad \frac{\partial A_n}{\partial t} + \epsilon J(\Psi, A_n) + \epsilon\frac{\mathrm{i}}{2}(\Delta\Psi)A_n - \frac{\mathrm{i}}{2}Bu_n\,\Delta A_n - \underbrace{\frac{\mathrm{i}}{8}Bu_n^2\,\Delta^2 A_n}_{\text{remove for } Bu_n \lesssim \epsilon^2} = 0. \tag{5.2}$$

The modulation of storm-excited inertial waves by an eddy field is a three-dimensional problem, an idealized example of which is represented by the numerical simulations presented in § 2. Through projection onto vertical modes, we have deconstructed this interaction into a set of two-dimensional problems, which, for reasonable dimensional values, may fall into different asymptotic regimes. The complete description of the three-dimensional problem requires a final summation over all of these modes and regimes. If a significant amount of the energy resides in one asymptotic regime, the overall behaviour of NIWs will be well described by the features of this regime (recall figure 2). We also note that although the two-dimensional problems reveal clear mechanisms for anticyclonic accumulation and the formation of small scales, no equivalently precise explanation for the increased vertical propagation speed of wave energy into the deep ocean is apparent. Nevertheless, it is broadly consistent with internal wave dynamics to say that smaller horizontal scale wave modes, produced through modulation, propagate faster, as may be inferred from (1.1). Thus for a given initial state, more energy in higher modes, with small Burger numbers, implies faster vertical propagation of wave energy.

Lastly, we note one speculation. We have shown that the nature of the wave-mean flow interaction depends on the ratio of the modal Burger and mean flow Rossby numbers. Taking the horizontal mean flow scale as the deformation scale, $L = NH/f$, this ratio is

$$\frac{Bu_n}{\epsilon} = \frac{NH}{n^2\pi^2 V_g}. \tag{5.3}$$

Because N decreases from mid-latitudes to the poles, one may expect to find more modes in the weak dispersion limit at higher latitudes, leading to more small-scale wave production and hence faster vertical propagation of wave energy.

Appendix A. Projecting (1.4) on baroclinic modes

We expand variables in (1.4) as

$$\boldsymbol{v}(\boldsymbol{x}, z, t) = \boldsymbol{v}_0(\boldsymbol{x}, t) + \sum_{n=1}^{\infty} \boldsymbol{v}_n(\boldsymbol{x}, t)\phi'_n(z), \quad w(\boldsymbol{x}, z, t) = \sum_{n=1}^{\infty} w_n(\boldsymbol{x}, t)\phi_n(z), \quad (A\,1a,b)$$

$$p(\boldsymbol{x}, z, t) = p_0(\boldsymbol{x}, t) + \sum_{n=1}^{\infty} \lambda_n^{-2} p_n(\boldsymbol{x}, t)\phi'_n(z), \quad b(\boldsymbol{x}, z, t) = \sum_{n=1}^{\infty} -p_n(\boldsymbol{x}, t)\tilde{N}^2(z)\phi_n(z),$$

$$(A\,2a,b)$$

where $\phi_n(z)$, solves the Sturm–Liouville problem with λ_n as the eigenvalues

$$\phi''_n + \lambda_n^2 \tilde{N}^2(z)\phi_n = 0, \quad \phi_n(0) = \phi_n(-1) = 0. \quad (A\,3a,b)$$

In the case of constant stratification, which is the case we consider in this paper, $\tilde{N}(z) = 1$, the solutions are $\phi_0(z) = 1$ and $\phi_{n>0}(z) = \sin(n\pi z)$, with eigenvalues $\lambda_0 = 0$ and $\lambda_{n>0} = n\pi$

Substitution into (1.4) and use of the orthogonality relation between the modes results in shallow water equations (1.6) for each baroclinic mode, $n \geqslant 1$.

Derivation of the Fourier cosine series, (2.2)

From the Fourier cosine series in (2.2), it immediately follows that

$$A_n = \frac{2}{H} \int_{-H}^{0} \exp\left(-\frac{z^2}{2h^2}\right) \cos\left(\frac{n\pi z}{H}\right) \mathrm{d}z \quad \text{and} \quad A_0 = \frac{2}{H} \int_{-H}^{0} \exp\left(-\frac{z^2}{2h^2}\right) \mathrm{d}z. \quad (A\,4a,b)$$

From the above expression, observe that the integrand involved in the calculation of A_n depends on n so that for each n an integral needs to be evaluated. Our goal is to derive an expression for A_n so that the n dependence can be removed from the integrand. We differentiate A_n with respect to n to obtain

$$\begin{aligned}
\frac{\mathrm{d}A_n}{\mathrm{d}n} &= \frac{2\pi h^2}{H^2} \int_{-H}^{0} \left[-\frac{z}{2h^2} \exp\left(-\frac{z^2}{2h^2}\right) \right] \sin\left(\frac{n\pi z}{H}\right) \mathrm{d}z \\
&= \frac{2\pi h^2}{H^2} \left[\exp\left(-\frac{z^2}{2h^2}\right) \sin\left(\frac{n\pi z}{H}\right) \right]_{-H}^{0} - \frac{2n\pi^2 h^2}{H^3} \int_{-H}^{0} \exp\left(-\frac{z^2}{2h^2}\right) \cos\left(\frac{n\pi z}{H}\right) \mathrm{d}z \\
&= -\frac{n\pi^2 h^2}{H^2} A_n.
\end{aligned} \quad (A\,5)$$

Thus we obtain

$$A_n = A_0 \exp \left(-\frac{n^2 \pi^2 h^2}{2H^2} \right) \tag{A 6}$$

and substituting the expression for A_0 from (A 4) we find the expression for A_n in (2.2). Observe that in this new expression for A_n, the integrand does not depend on n, as in (A 4).

Appendix B. Diagonalizing the RSW equations

Consider a forced linear RSW system, i.e. a generalized form of (1.6) as

$$\frac{\partial \boldsymbol{v}}{\partial t} + \hat{z} \times \boldsymbol{v} + \alpha \nabla h + \boldsymbol{F}^v = 0, \tag{B 1a}$$

$$\frac{\partial h}{\partial t} + \nabla \cdot \boldsymbol{v} + F^h = 0. \tag{B 1b}$$

Then the above set of equations can be transformed to obtain:

$$\mathscr{L} h = \nabla \cdot \frac{\partial \boldsymbol{F}^v}{\partial t} + \hat{z} \cdot (\nabla \times \boldsymbol{F}^v) - \left(\frac{\partial^2 F^h}{\partial t^2} + F^h \right), \tag{B 2a}$$

$$\mathscr{L} \boldsymbol{v} = \hat{z} \times \frac{\partial \boldsymbol{F}^v}{\partial t} - \frac{\partial^2 \boldsymbol{F}^v}{\partial t^2} - \alpha \nabla \times (\nabla \times \boldsymbol{F}^v) + \alpha \left(\nabla \frac{\partial F^h}{\partial t} - \hat{z} \times \nabla F^h \right), \tag{B 2b}$$

where $\mathscr{L} = (\partial/\partial t)((\partial^2/\partial t^2) + 1 - \alpha \Delta)$. This can be seen as follows.

Equation for h. Introducing $\zeta = \hat{z} \cdot \nabla \times \boldsymbol{v}$, the curl of (B 1a) gives

$$\frac{\partial \zeta}{\partial t} + \nabla \cdot \boldsymbol{v} + \hat{z} \cdot (\nabla \times \boldsymbol{F}^v) = 0 \tag{B 3}$$

and the time derivative of the divergence of (B 1a) gives

$$\frac{\partial^2}{\partial t^2} (\nabla \cdot \boldsymbol{v}) - \frac{\partial \zeta}{\partial t} + \alpha \Delta \frac{\partial h}{\partial t} + \nabla \cdot \frac{\partial \boldsymbol{F}^v}{\partial t} = 0. \tag{B 4}$$

Adding (B 4) + (B 3) gives

$$\frac{\partial^2}{\partial t^2} (\nabla \cdot \boldsymbol{v}) + \nabla \cdot \boldsymbol{v} + \alpha \Delta \frac{\partial h}{\partial t} + \hat{z} \cdot (\nabla \times \boldsymbol{F}^v) + \nabla \cdot \frac{\partial \boldsymbol{F}^v}{\partial t} = 0. \tag{B 5}$$

From (B 1b) we have

$$\nabla \cdot \boldsymbol{v} = -\frac{\partial h}{\partial t} - F^h \tag{B 6}$$

and finally using (B 6) in (B 5), we obtain (B 2a).

Equation for $\boldsymbol{v}$. The curl of (B 1a) gives

$$\nabla \times \frac{\partial \boldsymbol{v}}{\partial t} + (\nabla \cdot \boldsymbol{v})\hat{z} + \nabla \times \boldsymbol{F}^v = 0 \tag{B 7}$$

and using (B 6) gives

$$\nabla \times \frac{\partial \boldsymbol{v}}{\partial t} - \frac{\partial h}{\partial t}\hat{\boldsymbol{z}} - F^h\hat{\boldsymbol{z}} + \nabla \times \boldsymbol{F}^v = 0. \tag{B 8}$$

Taking the curl again and rearranging gives

$$\nabla \times \left(\nabla \times \frac{\partial \boldsymbol{v}}{\partial t} \right) + \hat{\boldsymbol{z}} \times \nabla \frac{\partial h}{\partial t} = \nabla F^h \times \hat{\boldsymbol{z}} - \nabla \times (\nabla \times \boldsymbol{F}^v). \tag{B 9}$$

From (B 1a) we have

$$\frac{\partial \boldsymbol{v}}{\partial t} = -\hat{\boldsymbol{z}} \times \boldsymbol{v} - \alpha \nabla h - \boldsymbol{F}^v. \tag{B 10}$$

Using this in the time derivative of (B 1a) gives

$$\frac{\partial^2 \boldsymbol{v}}{\partial t^2} = \hat{\boldsymbol{z}} \times \left(\hat{\boldsymbol{z}} \times \boldsymbol{v} + \alpha \nabla h + \boldsymbol{F}^v \right) - \alpha \nabla \frac{\partial h}{\partial t} - \frac{\partial \boldsymbol{F}^v}{\partial t}. \tag{B 11}$$

Rearranging after one more time differentiation gives

$$\frac{\partial}{\partial t} \left(\frac{\partial^2 \boldsymbol{v}}{\partial t^2} + \boldsymbol{v} \right) + \alpha \left(\nabla \frac{\partial^2 h}{\partial t^2} - \hat{\boldsymbol{z}} \times \nabla \frac{\partial h}{\partial t} \right) = \hat{\boldsymbol{z}} \times \frac{\partial \boldsymbol{F}^v}{\partial t} - \frac{\partial^2 \boldsymbol{F}^v}{\partial t^2}. \tag{B 12}$$

From (B 1b) one has

$$\nabla \frac{\partial^2 h}{\partial t^2} = -\nabla \left(\nabla \cdot \frac{\partial \boldsymbol{v}}{\partial t} \right) - \nabla \frac{\partial F^h}{\partial t}, \tag{B 13}$$

which on using $\nabla \times (\nabla \times \partial \boldsymbol{v}/\partial t) = \nabla(\nabla \cdot \partial \boldsymbol{v}/\partial t) - \Delta \partial \boldsymbol{v}/\partial t$ becomes

$$\nabla \frac{\partial^2 h}{\partial t^2} = -\left[\Delta \frac{\partial \boldsymbol{v}}{\partial t} + \nabla \times \left(\nabla \times \frac{\partial \boldsymbol{v}}{\partial t} \right) \right] - \nabla \frac{\partial F^h}{\partial t}. \tag{B 14}$$

Thus

$$\nabla \frac{\partial^2 h}{\partial t^2} - \hat{\boldsymbol{z}} \times \nabla \frac{\partial h}{\partial t} = -\left(\Delta \frac{\partial \boldsymbol{v}}{\partial t} + \nabla \times \left(\nabla \times \frac{\partial \boldsymbol{v}}{\partial t} \right) + \hat{\boldsymbol{z}} \times \nabla \frac{\partial h}{\partial t} \right) - \nabla \frac{\partial F^h}{\partial t}. \tag{B 15}$$

Using (B 9) in the above equation, we obtain

$$\nabla \frac{\partial^2 h}{\partial t^2} - \hat{\boldsymbol{z}} \times \nabla \frac{\partial h}{\partial t} = -\Delta \frac{\partial \boldsymbol{v}}{\partial t} - \nabla \frac{\partial F^h}{\partial t} - \nabla F^h \times \hat{\boldsymbol{z}} + \nabla \times (\nabla \times \boldsymbol{F}^v). \tag{B 16}$$

Finally, using (B 16) in (B 12) gives (B 2b).

REFERENCES

ABLOWITZ, M. J. 2011 *Nonlinear Dispersive Waves-Asymptotic Analysis and Solitons*. Cambridge University Press.

ALFORD, M.H, MACKINNON, J. A., SIMMONS, H. L. & NASH, J. D. 2016 Near-inertial internal gravity waves in the ocean. *Annu. Rev. Mar. Sci.* **8**, 95–123.

BALMFORTH, N. J. & YOUNG, W. R. 1999 Radiative damping of near-inertial oscillations. *J. Mar. Res.* **57**, 561–584.

CHAVANNE, C. P., FIRING, E. & ASCANI, F. 2012 Inertial oscillations in geostrophic flow: is the inertial frequency shifted by $\zeta/2$ or by ζ. *J. Phys. Oceanogr.* **42**, 884–888.

CHELTON, D. B., SCHLAX, M. G., FREILICH, M. H. & MILLIFF, R. F. 2004 Satellite measurements reveal persistent small-scale features in ocean winds. *Science* **303**, 978–983.

CRAIK, A. D. D. 1985 *Wave Interactions and Fluid Flows*. Cambridge University Press.

DANIOUX, E. & KLEIN, P. 2008 A resonance mechanism leading to wind-forced motions with a 2f frequency. *J. Phys. Oceanogr.* **38**, 2322–2329.

DANIOUX, E., VANNESTE, J. & BÜHLER, O. 2015 On the concentration of near-inertial waves in anticyclones. *J. Fluid Mech.* **773**, R2.

D'ASARO, E. A., ERIKSEN, C. C., LEVINE, M. A., NIILER, P., PAULSON, C. A. & VAN MEURS, P. 1995 Upper ocean inertial currents forced by a strong storm. Part I: data and comparisons with linear theory. *J. Phys. Oceanogr.* **25**, 2909–2936.

DYSTHE, K. B. 1979 Note on a modification to the nonlinear Schrödinger equation for application to deep water waves. *Proc. R. Soc. Lond.* A **369**, 105–114.

ELIPOT, S., LUMPKIN, R. & PRIETO, G. 2010 Modification of inertial oscillations by the mesoscale eddy field. *J. Geophys. Res.* **115**, C09010.

FALKOVICH, G. E. 1992 Inverse cascade and wave condensate in mesoscale atmospheric turbulence. *Phys. Rev. Lett.* **69**, 3173–3176.

FALKOVICH, G. E., KUZNETSOV, E. & MEDVEDEV, S. B. 1994 Nonlinear interaction between long inertio-gravity and Rossby waves. *Nonlinear Process. Geophys.* **1**, 168172.

FERRARI, R. & WUNSCH, C. 2009 Ocean circulation kinetic energy: reservoirs, sources and sinks. *Annu. Rev. Fluid Mech.* **41** (1), 253–282.

FOMIN, L. M. 1973 Inertial oscillations in a horizontally inhomogeneous current velocity field. *Izv. Atmos. Ocean. Phys.* **9**, 37–40.

GARRETT, C. & MUNK, W. 1979 Internal waves in the ocean. *Annu. Rev. Fluid Mech.* **11** (3), 339–369.

GILL, A. E. 1984 On the behavior of internal waves in the wakes of storm. *J. Phys. Oceanogr.* **14**, 1129–1151.

JOYCE, T. M., TOOLE, J. M., KLEIN, P. & THOMAS, L. N. 2013 A near-inertial mode observed within a gulf stream warm-core ring. *J. Geophys. Res.* **118**, 1797–1806.

KLEIN, P. & LLEWELLYN SMITH, S. G. 2001 Horizontal dispersion of near-inertial oscillations in a turbulent mesoscale eddy field. *J. Mar. Res.* **59**, 697–723.

KLEIN, P. & TREGUIER, A. M. 1995 Dispersion of wind-induced inertial waves by a barotropic jet. *J. Mar. Res.* **53**, 1–22.

LEE, D.-K. & NIILER, P. P. 1998 The inertial chimney: the near-inertial energy drainage from the ocean surface to the deep layer. *J. Geophys. Res.* **103** (C4), 7579–7591.

MOEHLIS, J. & LLEWELLYN SMITH, S. G. 2001 Radiation of mixed layer near-inertial oscillations into the ocean interior. *J. Phys. Oceanogr.* **31**, 1550–1560.

POLLARD, R. T. 1970 On the generation by winds of inertial waves in the ocean. *Deep-Sea Res. Oceanogr. Abstr.* **17** (4), 795–812.

POLLARD, R. T. 1980 Properties of near-surface inertial oscillations. *J. Phys. Oceanogr.* **10**, 385–398.

POLLARD, R. T. & MILLARD, R.C. JR. 1970 Comparison between observed and simulated wind-generated inertial oscillations. *Deep-Sea Res. Oceanogr. Abstr.* **17** (4), 813–816.

SILVERTHORNE, K. E. & TOOLE, J. M. 2009 Seasonal kinetic energy variability of near-inertial motions. *J. Phys. Oceanogr.* **39**, 1035–1049.

THOMAS, J. 2016 Resonant fast-slow interactions and breakdown of quasi-geostrophy in rotating shallow water. *J. Fluid Mech.* **788**, 492–520.

TRULSEN, K. & DYSTHE, K. B. 1996 A modified nonlinear Schrödinger equation for broader bandwidth gravity waves on deep water. *Wave Motion* **24**, 281–289.

VALLIS, G. K. 2006 *Atmospheric and Oceanic Fluid Dynamics*. Cambridge University Press.

WAGNER, G. L. & YOUNG, W. R. 2016 A three-component model for the coupled evolution of near-inertial waves, quasi-geostrophic flow and the near-inertial second harmonic. *J. Fluid Mech.* **802**, 806–837.

WHITT, D. B. & THOMAS, L. N. 2015 Resonant generation and energetics of wind-forced near-inertial motions in a geostrophic flow. *J. Phys. Oceanogr.* **45**, 181–208.

XIE, J. H. & VANNESTE, J. 2015 A generalised-lagrangian-mean model of the interactions between near-inertial waves and mean flow. *J. Fluid Mech.* **774**, 143–169.

YOUNG, W. R. & BEN JELLOUL, M. 1997 Propagation of near-inertial oscillations through a geostrophic flow. *J. Mar. Res.* **55**, 735–766.

ZEITLIN, V., REZNIK, G. M. & BEN JELLOUL, M. 2003 Nonlinear theory of geostrophic adjustment. Part 2. Two-layer and continuously stratified primitive equations. *J. Fluid Mech.* **491**, 207–228.

ZHAI, X., GREATBATCH, R. J. & EDEN, C. 2007 Spreading of near-inertial energy in a 1/12 model of the north atlantic ocean. *Geophys. Res. Lett.* **34**, L10609.

ZHAI, X., GREATBATCH, R. J. & ZHAO, J. 2005 Enhanced vertical propagation of storm-induced near-inertial energy in an eddying ocean channel model. *Geophys. Res. Lett.* **32**, L18602.